MID-CENTURY WARMING IN THE LOS ANGELES REGION

Part I of the "Climate Change in the Los Angeles Region" project

UCLA Institute of the Environment and Sustainability

LARC
Los Angeles Regional Collaborative
for Climate Action and Sustainability

Mid-Century Warming in the Los Angeles Region

Part I of the "Climate Change in the Los Angeles Region" project

Table of Contents

Abstract

Using a combination of dynamical and statistical downscaling techniques, we projected mid-21st century warming in the Los Angeles region at 2-km (1.2-mile) resolution. To account for uncertainty associated with the trajectory of future greenhouse gas emissions and other factors affecting the planet's energy balance, we examined projections for both "business-as-usual" (RCP8.5) and "mitigation" (RCP2.6) emissions scenarios of the Fifth Coupled Model Intercomparison Project. To account for the considerable uncertainty associated with choice of global climate model, we downscaled results for all available global models. For the business-as-usual scenario, we find that by the mid-21st century, the most likely warming is roughly 4.6°F averaged over the region's land areas, with a 95% confidence that the warming lies between 1.7 and 7.5°F. The high resolution of the projections reveals a pronounced spatial pattern in the warming: High elevations and inland areas separated from the coast by at least one mountain complex warm 20 to 50% more than the areas near the coast or within the Los Angeles basin. This warming pattern is especially apparent in summertime. The summertime warming contrast between the inland and coastal zones has a large effect on the most likely expected number of extremely hot days per year. Coastal locations and areas within the Los Angeles basin see roughly two to three times the number of extremely hot days, while high elevations and inland areas typically experience approximately three to five times the number of extremely hot days. Under the mitigation emissions scenario, the most likely warming and increase in heat extremes are somewhat smaller. However, the majority of the warming seen in the business-as-usual scenario still occurs at all locations in the most likely case under the mitigation scenario, and heat extremes still increase significantly. Therefore adaptation to a changing climate over the next few decades is likely to be inevitable in the Los Angeles region.

1 Project Background

The greater Los Angeles area is home to nearly 18 million people, who together account for nearly $750 billion in economic activity every year (U.S. Metro Economies -- Gross Metropolitan Product with Housing Update, 2007). It is therefore critical to assess climate change in the region and determine its impacts at space and time scales relevant for municipal planning and policymaking. The "Climate Change in the Los Angeles Region" project is meant to facilitate this assessment activity, and provide a quantitative foundation for a regional action plan in the areas of climate change adaptation and mitigation. The project relies on output from publicly-available global climate change simulations. These simulations are state-of-the-art, but because they are global, their resolution (roughly 200 km on average) is too coarse to provide meaningful information about climate change at the regional scales of interest for this project. Therefore we undertook additional high-resolution simulations to regionalize the climate change signals implicit in current global simulations. This particular study focuses on the changes in near-surface temperature and associated heat extremes. Other critical aspects of climate change in the region, including those related to precipitation, snowpack and surface hydrology, Santa Ana winds, and low clouds are presented in companion studies.

2 The Global Climate Simulations

The global climate model simulations noted above are widely used for understanding and projecting future global climate change resulting from increases in atmospheric concentrations of greenhouse gases and other factors affecting the planet's energy balance. We rely on a recently-released data archive of coordinated global climate change experiments, known as the Fifth Coupled Model Intercomparison Project (CMIP5). At the time of this study, CMIP5 contains output from roughly two dozen state-of-the-art global climate models ("general circulation models" or GCMs) developed at leading climate research centers around the world. This data set allows the scientific community to address outstanding questions surrounding climate change. It also forms the basis of the forthcoming Fifth Assessment Report (AR5) of the United Nations Intergovernmental Panel on Climate Change (IPCC). CMIP5 provides a multi-model context for understanding the relationship between the factors affecting the planet's energy balance,

including greenhouse gas emissions and climate change. It also provides a range of climate responses across the different GCMs under multiple greenhouse gas emissions scenarios (Taylor et al., 2009).

A set of future emissions scenarios known as Representative Concentration Pathways (RCPs) has been adopted by the organizers of the CMIP5 archive (Moss et al., 2008, Meinshausen et al., 2011). Four RCPs have been chosen, RCP2.6, RCP4.5, RCP6, and RCP8.5. The names of the scenarios correspond to the approximate radiative forcing they would produce at the end of the 21st century (2.6, 4.5, 6.0, and 8.5 watts per square meter [$W \cdot m^{-2}$], respectively). The radiative forcing up to the year 2100 is shown in Fig. 1a for each scenario, with the historical forcing also shown up to the year 2005. RCP2.6 is representative of a "mitigation" scenario in which greenhouse gas emissions peak roughly within the next two decades. The resulting carbon dioxide (CO_2) equivalent concentrations, encompassing the net effect of all anthropogenic forcing agents, reach a maximum level of approximately 460 parts per million by volume (ppmv) around 2050 and decline thereafter to approximately 420 ppmv by 2100 (Fig. 1b). Total radiative forcing relative to pre-industrial levels peaks at about 3 $W \cdot m^{-2}$ in the middle of the 21st century and declines to 2.6 $W \cdot m^{-2}$ by 2100. In stark contrast to RCP2.6, RCP8.5 represents a "business as usual" scenario, where greenhouse gas emissions continue to increase throughout the 21st century. The result is a total radiative forcing of 8.5 $W \cdot m^{-2}$ and CO_2-equivalent concentrations greater than 1200 ppmv by 2100. While RCP8.5 is the most aggressive emissions scenario, it corresponds most closely to emission trends over the past decade. Between the "mitigation" scenario of RCP2.6 and the "business as usual" scenario of RCP8.5 are two "stabilization" scenarios, RCP4.5 and RCP6. In this study, however, we focus on the climate response to the two end-member scenarios at either extreme, i.e., RCP8.5 and RCP2.6, to sample efficiently the full range of climate outcomes associated with potential future emissions.

The global-mean surface air temperature response to the RCP2.6 and RCP8.5 scenarios seen in the CMIP5 GCMs is shown in Fig. 1c. (Table 1 summarizes the available global climate models used in this study from the CMIP5 archive.) For both scenarios, there are clearly significant model-to-model differences in the warming

response over the course of the 21st century. These variations arise principally from differences in the GCMs' spatial resolutions and physical parameterizations. These parameterizations are formulated at the various modeling centers. They represent processes occurring at scales smaller than the GCM grid scale, especially those associated with cloud, the atmospheric boundary layer schemes, and oceanic eddies. Thus the outcomes seen in Fig. 1c approximately represent the range of possible warming that results when the various ways of constructing a physically-based model of the climate system are implemented in a climate change projection. For this reason, we interpret the range of warming outcomes as the climate change uncertainty associated with a given emissions scenario. We also interpret the average response of all the GCMs for a given emissions scenario (the "ensemble mean") as the most likely outcome for that scenario. This assumes the GCMs randomly sample the uncertainty space associated with the simulated response to anthropogenic forcing. This approach to likelihood and climate change uncertainty quantification has been used in previous IPCC reports (Meehl et al., 2007) and will be used by the IPCC-AR5.

We focus on two time periods in this study: A "baseline" (1981-2000) and a "future" (2041-2060). These two periods are shaded in Fig. 1. Mid-century climate change relative to the late 20th century can be quantified by calculating the differences between the future and baseline periods. By this metric, the GCMs generally show significant warming in both the RCP2.6 and RCP8.5 scenarios at the global scale. This validates our choice for the future time period, which must be far enough in the future to allow for unambiguous climate change signals, but still within a time horizon appropriate for policymakers and local stakeholders. There is a visible systematic difference between the two scenarios in the typical global-scale warming. However, the least sensitive GCMs show about as much warming under the RCP8.5 scenario as the most sensitive ones under RCP2.6. Thus at mid-century the uncertainty range associated with the RCP8.5 scenario overlaps that of the RCP2.6. As we will see in Section 7, this behavior is reproduced when the GCMs are downscaled to the Los Angeles region. It is not until the latter third of the 21st century that the range of simulated climate change associated with RCP8.5 becomes entirely distinct from that associated with RCP2.6.

3 The Need for Dynamical and Statistical Downscaling

The typical resolution of current GCMs (~200 km, see Table 1) is much too coarse to accurately characterize climate variability and change at scales relevant to municipal planning and policymaking. This is especially true in regions with complex topography and meandering coastlines, such as the Los Angeles region. Because of their relatively coarse resolution, GCMs simulate regional-scale climate dynamics poorly, including local circulations shaped by topography, land-sea breezes and mountain/valley circulation systems, and orographic precipitation. All of these phenomena have significant manifestations in the Los Angeles region. Indeed, previous studies have confirmed that taking into account climate processes with spatial scales of a few km is important for simulating and understanding current climate variability in the region and in the rest of the state of California (e.g., Cayan 1996, Conil and Hall 2006, Hughes et al., 2007, Lundquist and Cayan, 2007, Cayan et al., 2008, Hughes et al., 2009).

To obtain reliable climate change information at the regional-scale, we employ both dynamical and statistical techniques to downscale the relatively coarse-resolution climate information from GCMs to much finer spatial scales. Dynamical downscaling refers to the use of regional numerical models to solve the equations of the atmosphere (and in some cases the ocean) over a limited-area at high resolution, typically a few to tens of km. Apart from their regional focus and higher resolution, these models are very similar to GCMs. The regional models are typically driven by coarse-resolution GCM output or reanalysis data along the boundaries. This allows for simulations of fine-scale physical processes that are consistent with the evolution of the atmosphere encoded in the larger-scale data product. Dynamical downscaling has been widely applied over many regions to examine a range of climate change impacts (Leung and Ghan, 1999, Giorgi et al., 2001, Wang et al., 2004, Chin 2008). This approach has already proven valuable in providing information on California climate change, including impacts on temperature, snowpack, and the hydrologic cycle (Leung et al., 2003, Cayan et al., 2008, Caldwell et al., 2009, Qian et al., 2010, Pan et al., 2011). The other downscaling technique we use—statistical downscaling—relies on empirical mathematical relationships between the large-scale climate predictors and the climate variables at regional scale. These

relationships are then used to project regional climate change given the change at larger-scales (von Storch et al., 1993, Wilby et al., 2004).

The main advantage of dynamical downscaling is that the regional numerical model produces a climate change response driven purely by its own internal dynamics. Unlike a climate response produced by statistical downscaling, a dynamically downscaled response is in no way pre-determined by any assumptions about the relationship between regional climate and climate at larger scales. However, this benefit of dynamical downscaling must be balanced against its very high computational cost. Generally a regional climate change simulation will require several months of computer time. Since it is highly impractical to dynamically downscale every global climate model forced by each emissions scenario, it is nearly impossible to fully characterize climate change uncertainty with dynamical techniques alone. For this reason we employ statistical techniques, which have the advantage of negligible computational costs, in conjunction with dynamical downscaling. The basic idea is undertake dynamical downscaling for a single GCM and a single emissions scenario (RCP8.5), and then use that simulation to diagnose mathematical relationships between the large-scale climate change seen in the GCM and the dynamically-downscaled response. These relationships then become the foundation of a statistical model that efficiently downscales the other GCMs forced by RCP8.5, as well as all the GCMs when they are forced by RCP2.6. Combining dynamical and statistical downscaling techniques in this way allows us to incorporate the most important dynamical processes shaping regional climate change *and* quantify approximate uncertainties associated with the various global climate projections and the two end-member emissions scenarios.

4 Dynamical Downscaling Methods

4.1 WRF Modeling Framework

To perform the dynamical downscaling, we use the Weather Research and Forecasting Model (WRF; Skamarock et al., 2008) version 3.2. WRF is a community mesoscale model, developed by the National Center for Atmospheric Research (NCAR). It is designed for use on regional grids for a range of applications, such as weather forecasts and climate simulations. It consists of a fully compressible nonhydrostatic dynamical

core with high-order, conserving numerical techniques, and a full suite of physics parameterizations. We optimized this regional model for the California region with sensitivity experiments using various parameterizations, paying particular attention to the model's ability to simulate low cloud in the marine boundary layer off the California coast. Our parameterization choices are the follows: Kain-Fritsch (new Eta) cumulus scheme (Kain, 2004); Yonsei University boundary layer scheme (Hong et al., 2006); Purdue Lin microphysics scheme (Lin et al., 1983); Rapid Radiative Transfer Model longwave radiation (Mlawer et al., 1997); Dudhia shortwave radiation schemes (Dudhia, 1989). We also use the Noah land surface model (Chen and Dudhia, 2001) to simulate land surface processes including vegetation, soil, snowpack and exchange of energy, momentum and moisture between the land and atmosphere.

The domains for the simulations are shown in Fig. 2. To gradually bridge the scales of the coarser resolution datasets used to force regional model at its lateral boundaries, successively higher resolution domains must be nested within one another. Each of the outer domains provides lateral boundary conditions to the domain nested within it, until eventually the region of interest is covered at the highest resolution. In the configuration used for this study, there are 3 nested domains. The outermost domain covers the entire state of California and the adjacent ocean at a horizontal resolution of 18 km, the middle domain covers roughly the southern half of the state at a horizontal resolution of 6 km, while the innermost domain encompasses Los Angeles county and surrounding regions at a horizontal resolution of 2 km. In each domain, all variables in grid cells closer in the horizontal than five cells from the lateral boundary are relaxed towards the corresponding values at the boundaries separating the domains. This procedure ensures smooth transitions across these boundaries. Each domain has 43 sigma-levels in the vertical. To provide a better representation of surface and boundary layer processes, the model's vertical resolution is enhanced near the surface, with 30 sigma-levels below 3 km. Fig. 3 shows a blow-up of the topography and coastlines for the innermost domain at its native 2-km resolution. The main features of both the topography and coastlines are represented well at this resolution.

Using this model configuration, we performed a "baseline" simulation whose purpose is two-fold: (1) to validate the model's ability to simulate regional climate, and (2) to provide a baseline climate state against which a future climate simulation could be compared. This simulation is a dynamical downscaling of a publicly-available, coarse-resolution (32 km) archive of the weather and climate variations over North America during the baseline period (1981-2000). The simulation is designed to reconstruct the actual regional weather and climate variations that occurred during this time period at 2-km resolution, and its output can be compared to available observations for model validation purposes. The coarse-resolution archive used to force the regional model is the National Centers for Environmental Prediction 3-hourly North America Regional Reanalysis (NARR) data. This dataset provides lateral boundary conditions at the outer boundaries of the outermost domain (shown in Fig. 2). It also provides surface boundary conditions over the ocean (i.e., sea surface temperature) in each of the three domains.

Using the same model configuration, we also performed a second dynamical downscaling experiment whose purpose is to simulate a regional climate state during the "future" period (2041-2060). The output of this experiment can be compared to the baseline simulation to measure simulated regional climate change. As noted in Section 2, the goal of this study is to provide information about regional climate change for a time slice centered at the middle of the 21st century for the RCP8.5 and RCP2.6 emissions scenarios. Accordingly, we downscale future coarser-resolution global climate simulation output corresponding to this time period and the RCP8.5 emissions scenario. (We recover the RCP2.6 results with statistical downscaling techniques, as discussed in Section 5.2 below.) The global model we chose is NCAR Community Climate System Model version 4 (CCSM4, Gent et al., 2011).

To produce future climate boundary conditions for the regional model, we quantified the differences in CCSM4 monthly climatology between the future and baseline periods. These differences are the climate change signals of interest that develop in the CCSM4 simulation. All variables are included in the calculation of the climate change signal (i.e., 3-dimensional atmospheric variables such as temperature, relative humidity, zonal and meridional winds, and geopotential height and 2-dimensional surface

variables such as temperature, relative humidity, winds and pressure). On a monthly-varying basis, we add these climate change signals to the NARR reanalysis data corresponding to the baseline period. Thus, we perturbed the NARR baseline data with climate change signals provided by CCSM4. We used this perturbed NARR data to construct the boundary conditions imposed on the outermost domain of the regional model. The resulting simulation can then be compared directly with the baseline regional simulation to assess the impact of the CCSM4 climate change signals when they are downscaled. It should be noted that because we downscaled the climate change signal in CCSM4 rather than the raw CCSM4 data, we did not regionalize the hour-to-hour and day-to-day variability in CCSM4. Accordingly, we cannot provide any information about how climate change may affect higher order statistics of variability such as skewness and kurtosis, except insofar as those variability statistics are affected by the internal atmospheric dynamics of the regional model. CO_2 levels were also increased in WRF to match the changes in CO_2-equivalent radiative forcing in the RCP8.5 scenario averaged over the future period compared to the baseline.

For both baseline and future climate simulations, the model output consists of snapshots of 2-dimensional variables every 3 hours and 3-dimensional variables every 6 hours.

4.2 Validation of Baseline Climate Simulation

In this section, we validate the regional model's ability to reproduce climate variations within the innermost domain when the available coarse-resolution information about the actual history of the atmosphere is imposed on it. This is done by comparing the baseline climate simulation output to available point measurements. The network of point measurements is shown in Fig. 3. Quality-controlled, hourly, near-surface meteorological observations from 24 weather stations were obtained from the National Climatic Data Center (NCDC; http://www.ncdc.noaa.gov/oa/ncdc/html). These observations include land and ocean buoy locations. Since the focus of this study is the warming component of climate change, the validation exercise is limited to comparison of simulated and observed temperature variations. Validation of other aspects of the simulation is reserved for studies examining their response to climate change.

Fig. 4 shows the baseline simulation's geographical distribution of temperature for each phase of the seasonal cycle. The values presented here are climatological averages over the entire baseline simulation period (1981-2000). A distinct seasonal cycle is simulated, with the coldest temperatures occurring throughout the region during the winter and the warmest during the summer. Temperature generally decreases with elevation in all seasons, so that mountain areas are easily discernible in all four panels of Fig. 4. The most dramatic seasonal temperature fluctuations occur in the southern San Joaquin Valley and Mojave Desert, ranging from approximately 45°F during the winter to above 80°F during summer, followed by the mountains, which typically have a seasonal range of about 25°F. During the summer, the Southern California Bight is cooler than the southern San Joaquin Valley and high desert, while the opposite is true in winter. Thus, a reversal in the land-sea temperature contrast between summer and winter is simulated. This land-sea temperature contrast has important weather and climate implications for the region, and is involved in the region's temperature response to climate change, as we will discuss. Moderated by marine air periodically flowing inland, inter-seasonal temperature ranges in the coastal regions are relatively small (15°F). As we will also discuss below, the moderating influence of the ocean on the temperature of the coastal zone also affects the future warming this area experiences.

The network of available point measurements seen in Fig. 3 is far too sparse to adequately characterize spatial patterns such as those seen in Fig. 4. Still, it can be used to assess the realism of the spatial patterns of Fig. 4. The point measurements are located in a variety of elevations and distances from the coast, and are numerous enough to provide a sampling of the range of temperatures seen across the region. However, both the length and completeness of the observational temperature record vary by location. All observational points have relatively complete records after 1995. Because the baseline simulation ends in 2000, we focus on the period between 1995 and 2000 in our comparison between observations and model.

Fig. 5a compares climatological temperature for observational locations and the nearest model grid point, providing an assessment of the realism of the spatial and seasonal patterns seen in near-surface temperature climatology of Fig. 4. The seasonal

cycle of temperature simulated by the model is highly consistent with observations. The seasonal shifts in temperature are nearly identical at the observational locations and the nearest model grid points. In addition, within each season, the observed climatological temperatures are highly correlated with their simulated counterparts across the region. This confirms that for each season, the model simulates the spatial variations in climatological temperature reasonably well. The model quality is particularly high in summer and winter. During the transition seasons, the model and observations are still in broad agreement, though the correlation is somewhat lower. In Fig. 5b, we validate the model's ability to simulate temporal variability in temperature at monthly time scales and longer, with the seasonal cycle removed. At each observational location, the observed near-surface temperature variations are very well-correlated to the corresponding simulated variations, often with nearly perfect correlations greater than 0.90.

Fig. 5 demonstrates that the model gives approximately the right spatial and temporal variations in near-surface temperature at specific point locations where trustworthy observational data area available. This gives a high degree of confidence that the model is also producing the correct temperature variations in the rest of the region, where observations are absent. And most importantly for this study, it gives confidence that when it comes to near-surface temperature, the model provides a realistic downscaling of the regional pattern implicit in the coarser resolution data set. Thus the dynamically-downscaled climate change patterns we will present here are very likely a true reflection of the regionalized climate signal of the global model. Of course, we have only evaluated the quality of the near-surface temperature fields in the baseline simulation, and this is but one aspect of overall model quality.

4.3 Dynamically-Downscaled Surface Warming Patterns

In this section, we examine the climatological difference in near-surface air temperature between the baseline and future dynamical downscaling simulations. This is the regional expression of the CCSM4 RCP8.5 climate change signal, as generated by the WRF model.

The annual mean near-surface warming is illustrated in Fig. 6. The warming magnitude generally increases with distance from the coastline. It is about 1.5°F in the

Southern California Bight, 2°F in the urban coastal zone, 3°-3.5°F in the desert interior, and up to 4°F at the higher elevations of the region's mountain complexes. A striking feature of Fig. 6 is that the warming is somewhat suppressed in the coastal zone compared to the other land areas. This is likely due to the same factors that moderate the seasonality of temperature in the coastal zone in the baseline climate. These factors include, but are not limited to: (1) The land/sea breeze, which brings marine air and its characteristics to the coastal zone on a daily basis and (2) The fact that marine air passes more easily over this relatively low-elevation zone simply because of the absence of topographic barriers. Clearly the ridges of the mountain complexes ringing the coastal zone create a formidable barrier to the penetration of marine air masses, as the warming becomes larger passing over these ridges to the interior. Aside from topography, land surface characteristics could be another key factor influencing the warming. It seems likely that the dryness of the desert interior is a large contributor to the warming there, as the increased energy input from the anthropogenic forcing is mostly balanced by an increase in sensible heat fluxes and hence is associated with a large temperature increase. It is plausible that the unique surface thermal properties of urban areas (e.g. heat capacity, emissivity, conductivity) could also affect the warming there. While these properties are included in the Noah land surface model, there is little evidence that they result in a differentiated urban effect, because the warming in the urbanized coastal zone is so similar to that over the coastal ocean.

The overwhelming impression is that the warming pattern is controlled by three factors: (1) the warming over the ocean, essentially inherited from CCSM4, (2) the warming over the desert, also inherited from CCSM4 but modulated by the Noah land surface model's calculation of surface energy balance there, and (3) WRF's simulation of local atmospheric dynamics, especially the land/sea breeze and the effect of local topography on air masses as they make their way through the region. This final factor determines the outcome of the competition between the ocean and desert warming signals at every location within the region. There is one additional noteworthy element of the warming pattern in the WRF downscaling of CCSM4. The warming pattern at high elevations is generally larger. In fact the greatest warming of the entire region is seen at

14

the tops of the San Gabriel and San Bernadino mountain complexes. We discuss the origin of this signal below.

Seasonality of the near-surface warming is shown in Fig. 7. Over the ocean, the warming is about 1.5°F all year round. Over land, by contrast, much more warming is seen in summer and fall compared to the other two seasons. The spatial distributions of warming in summer and fall also resemble another, with a large contrast between land and ocean. The main reason the most warming over land is seen in summer is that the land surface has dried out at this time of year. Increase in sensible heat fluxes is virtually the only way for the land surface to balance the extra energy it receives from the atmosphere in conjunction with climate change. Thus surface and surface air temperature must increase significantly. This effect increases going away from the coast, as the influence of marine air masses and soil moisture both decrease. In the coastal zone, the warming is about 2.5°F, increasing to 5°F in the Mojave Desert. This pattern persists throughout the fall months. The overall warming over land in the fall may be less than in the summer because the land surface occasionally becomes moistened toward the end of the fall as storms begin to arrive in the region, and evaporative processes offer additional ventilation of the surface. In both summer and fall, the warming is somewhat greater at high elevations. This signal arises because in CCSM4, the overall summer and fall warming in the entire subtropical atmosphere increases with height (not shown). Locations in the Los Angeles region high enough to rise above the main portion of the atmospheric boundary layer are affected by this enhanced warming signal.

The continuing moistening of the land surface as the wet season proceeds further reduces the warming contrast between land and ocean in the winter and then spring. During these two seasons, a small warming (~2°F) is simulated in the San Joaquin Valley and coastal regions with an additional ~0.5°F warming in inland areas. Greater warming at high elevations is also seen in winter and spring. This may be partly due to the greater warming with height in the global simulations, an effect noted previously. However, it may also be due to local snow albedo feedback. At high elevations snow is often found in the baseline climate during winter and spring, mainly over the San Gabriel, San Bernadino and San Jacinto Mountains. There is less snow in the future climate mainly

15

because of less snowfall and more snow melt (not shown). The decreased snow cover leads to more surface absorption of solar radiation, and hence more local warming. The strong warming signals over the mountains in spring, when there is more solar radiation and snow starts melting, are particularly likely to be linked to local snow albedo feedback. The warming at these high-elevation locations is as large as 3.5°F.

5 Statistical Downscaling Methods

5.1 Statistical Model Development

The warming patterns of Figs. 6 and 7 illustrate the necessity of dynamical downscaling to obtain information about climate change in the Los Angeles region. Several dynamical effects clearly influence the warming pattern, and these are therefore very difficult to assess without a dynamical model. They include: (1) the local topographically-modified atmospheric circulation, which plays a key role in determining the relative influence of marine and desert air masses and their warming characteristics at any particular location, (2) the geographical and seasonal variation in surface properties, especially the seasonal variation in soil moisture, which plays a large role in the seasonality of warming in the desert interior, and (3) the degree to which high-elevation locations rising above the main portion of the atmospheric boundary layer are influenced by the enhanced warming with height found throughout the subtropical atmosphere in the global model. Ideally we could quantify the spread in our prediction of the regional warming signal by dynamically downscaling all of the GCMs in the CMIP5 archive. However, this is highly impractical, as discussed in Section 1. Instead we use the dynamical downscaling we have done to develop a statistical model describing the mathematical relationship between the low-resolution CCSM4 warming signal and its high-resolution dynamical-downscaled counterpart. This relationship can then be used to downscale the other global models, approximating the warming pattern that would occur if the other global models were downscaled dynamically with WRF.

Consistent with the discussion in Section 4.3, we identified three principal characteristics in the global model simulation that govern the high-resolution spatial pattern of the warming in the WRF downscaling of the global model. The first and most obvious is the surface warming in those few grid points in the global simulation nearest

to the WRF 2-km domain. WRF inherits this overall warming directly from the global model. The second characteristic is the surface warming contrast between ocean and desert areas. The overall contrast is largely controlled by the global model, but local mechanisms described in the above paragraph determine whether a particular location has warming that is more "ocean-like" or "desert-like". For elevations below the main part of the atmospheric boundary layer, these first two characteristics are the main factors controlling the temperature change. However, for elevations above the main part of the atmospheric boundary layer, the temperature change is strongly controlled by the change in warming with height in the global model throughout the subtropical atmosphere, a third principal global model characteristic. The assumptions of our statistical model therefore reflect our belief that the WRF warming is determined by these three characteristics of the global model.

To state these assumptions more explicitly: (1) If a different GCM were dynamically downscaled, the regional mean of resulting warming pattern would differ from the regional mean of the CCSM4-WRF warming pattern by the difference in the regional means of the GCM and CCSM4. (2) The resulting warming pattern would share the same distribution of ocean and desert influences as CCSM4-WRF, because the local surface and atmospheric dynamics creating that pattern will be very similar, but that pattern will be scaled by ratio of the other GCM's land-sea warming contrast to that of CCSM4. (3) At elevations above the main part of the atmospheric boundary layer (greater than 1200 m), the warming pattern would reflect the differential warming with height in the GCM. Thus our statistical model takes as input the following parameters extracted from the GCM warming pattern: the regional mean warming, the land-sea warming contrast (i.e., the difference in warming between the inland and ocean regions), and the change in the lapse rate at high elevations. The output is a warming pattern whose regional average is higher or lower than that of CCSM4-WRF depending on how much higher or lower the global model's regional warming is relative to CCSM4, and whose spatial pattern of warming has been "dialed up" or "dialed down" depending on how large the GCM's land-sea warming contrast and lapse rate change are compared to CCSM4. A schematic of the statistical model is shown in Fig. 8, and a more detailed description of the statistical model is provided in the Appendix.

5.2 Regional Surface Warming Patterns associated with other GCMs

In this section, we apply the statistical model described in the previous section to compute regional warming patterns for each GCM under the RCP8.5 emissions scenario.

To provide some background on the GCMs' range in the first two critical input parameters for the statistical model, Fig. 9 shows a scatterplot of the regional-mean warming vs. the land-sea warming contrast in the 18 CMIP5 models. The regional-mean warming ranges from about 2°F to 6.5°F—a large intermodel spread. Models differ so much in the overall warming for two reasons. First, global climate sensitivity may vary across the models. Simulated transient global climate sensitivity is primarily determined by how radiatively-active components of the global climate system such as snow, ice, cloud and water vapor respond to a changing climate. Second, the rate of oceanic heat uptake may play a large role in determining how much transient warming occurs. Models used in the previous IPCC assessment reports exhibit a large intermodel spread in all these processes, creating a spread in transient global climate sensitivity (Bony et al., 2006, Boé et al., 2009, Winton et al., 2010). We expect the CMIP5 models to behave similarly. At the regional scale, GCMs may also differ in the way the large-scale atmospheric and oceanic circulation distributes the warming throughout the globe. This could cause a difference between two GCMs in the overall warming in the Los Angeles region, even if the two GCMs have the same global-mean warming.

In the vicinity of the Los Angeles region, warming over land is greater than warming over ocean in all models (Fig. 9). The land-sea contrast in mid-latitude warming is a feature of anthropogenic climate change that is well-known and well-understood. The smaller warming over ocean is generally attributed to the consistent availability of water for evaporative damping of surface temperature, and the very large effective heat capacity of seawater. Over land, by contrast, the effective heat capacity is relatively small. Also, when the soil is unsaturated, the surface temperature response to anthropogenic forcing must become large enough to generate enough sensible heat flux to balance the additional forcing. This is what leads to the well-established mid-latitude summertime drying and warming signal in GCMs (e.g., Manabe et al., 1981, Sutton et al., 2007). Climate feedbacks over either land or ocean may also enhance or attenuate this

contrast, depending on the model. For example, summertime warming over mid-latitude land areas is largely controlled by snow albedo feedback, whose strength varies significantly across GCMs (Hall et al., 2008). Warming over the subtropical North Pacific, by contrast, is likely affected by large intermodel variations in low cloud feedback (Bony et al., 2006), and their footprint in this zone. Together, these factors lead to a large intermodel spread in the land-sea warming contrast of about 1°F to 3.5°F.

The dots in Fig. 9 are also color-coded by the value of the third parameter—the annual-mean change in the lapse rate over the North Pacific adjacent to the California coast. These values vary from almost no lapse rate change to a greater warming at elevations corresponding to the top of the highest mountains in the region of more than 1°F (compared to the top of the atmospheric boundary layer). The large-scale lapse rate generally decreases because subtropical air parcels above the boundary layer mostly originate as air parcels detrained from tops of tropical convective towers, much higher in the atmosphere. Because of the decrease of the moist adiabatic lapse rate with temperature within the tropical convective towers, anthropogenic warming at these altitudes is larger than at lower altitudes. Due to their mostly tropical origin, subtropical air parcels above the boundary layer retain this signature of enhanced tropical warming aloft. (See Held and Soden (2000) for more details on this process.) Thus the spread in this parameter may be related to intermodel variations in the typical height changes of tropical convective towers or other aspects of the large-scale tropical circulation.

The ensemble-mean of the overall regional warming and the land-sea warming contrast over the 18 GCMs is also shown in Fig. 9. Clearly, the ensemble-mean values do not correspond to those of any particular model. Thus no single GCM is representative of the important processes shaping climate change in the Los Angeles region, and all are necessary to map out the uncertainty space implicit in the GCM ensemble. CCSM4 lies in the top-left corner of the distribution, with relatively small regional-mean warming, but a large land-sea warming contrast. Clearly it would be very misleading to base conclusions about climate change in the Los Angeles region exclusively on the dynamically-downscaled CCSM4 results.

Fig. 10 shows the regional-mean warming, land-sea warming contrast and lapse

rate change for the four seasons. In the ensemble-mean, the regional-mean warming (Fig. 10a) is greater in summer and fall (~4.5°F) than winter and spring (~3.5°F). The ensemble-mean land-sea warming contrast is greatest in summer (~2.5°F), smallest in winter (1°F), and in between in spring and fall (Fig. 10b). Large summertime warming over land in most GCMs is the likely reason both the overall warming and land-sea warming contrast are greatest in summertime. The lapse rate change (Fig. 10c) is positive in nearly all models and all seasons, indicating greater warming in the free troposphere than in the main part of the atmospheric boundary layer of about 0.5°F. The regional-mean warming for each season exhibits a three-to-four-fold intermodel spread, similar to the spread in the annual-mean warming seen in Fig. 9. The land-sea warming contrast likewise exhibits a significant intermodel spread. Finally, the lapse rate change also varies significantly from model to model, and from season to season. Again, CCSM4 is not generally in the center of the distributions of any of the parameters for any of the seasons.

Using the three parameters from each of the GCMs as input to the statistical model, we derive seasonal surface warming patterns for each GCM over the Los Angeles region. Fig. 11 shows the resulting annual-mean surface warming patterns (i.e. when these seasonal patterns are averaged over the whole year). A general warming is seen throughout the region and in every model, and the warming is generally largest in the inland desert area, while smallest over the ocean, consistent with information shown in Figs. 9 and 10. However, the magnitude of the warming at a particular location differs significantly from model to model. The largest intermodel differences are seen in the Mojave Desert, where the warming ranges from 3°F to 6°F. The coastal region also exhibits a comparable intermodel variation in surface warming, ranging from 2°F to 5°F. The smallest differences are seen over the Southern California Bight. These variations are the regional expressions of the intermodel differences in the regional-mean warming and the land-sea warming contrast seen in Figs. 9 and 10.

6 Mean Surface Warming

6.1 Annual-mean Warming Pattern

The annual-mean warming averaged over all 18 downscaled regional patterns (ensemble mean) for the RCP8.5 scenario is shown in Fig. 12b.We deem the ensemble-mean quantity to be the most likely value for the warming in the region, as discussed in Section 2. Figs. 12a and c provide upper and lower bounds of this warming. These bounds correspond to an approximate 95% confidence interval, calculated statistically based on the range of responses associated with the GCMs. The ensemble-mean warming shows that warmer temperatures are expected across the entire region, with a regionally-averaged warming of about 4.3°F, including both land and ocean points. The least amount of warming (~3.5°-4°F) is seen over the ocean, while slightly larger warming (~4°-4.5°F) occurs across the urban coastal zone, and the greatest warming (~4.5°-5°F) is found throughout the interior and desert zones. The ensemble-mean temperature changes across the entire region are greater than the corresponding annual-mean changes projected in the WRF dynamical downscaling simulation (shown in Fig. 6), while the ensemble-mean has a weaker land-sea warming contrast. These results are consistent with the relationship between the large-scale climate parameters of CCSM4 and those of the other models illustrated in Fig. 9.

Averaged over the region, the uncertainty in the annual-mean warming (i.e., the difference between the upper and lower bounds shown in Figs. 12a and c) is substantial—5.6°F. It is possible, though not likely, that relatively mild warming of about 1.5°F on a regionally-averaged basis would occur, and it is equally possible, though again, not likely, that a rather severe regional warming of nearly 7°F would materialize.

6.2 Seasonality of the Warming Pattern

The seasonality of the ensemble-mean warming for the RCP8.5 scenario is shown in Fig. 13. The patterns in this figure, and the reasons for them, are similar to those of the WRF-CCSM4 dynamically-downscaled warming seen in Fig. 7, with two notable exceptions. First, the warming is generally larger in all seasons. Second, whereas the warming over the ocean is similar in all seasons in the WRF-CCSM4 simulation, the ensemble-mean oceanic warming exhibits a pronounced maximum in fall, being approximately 1.5ºF

greater than in the other seasons. This oceanic seasonal warming pattern is a feature inherited from the GCMs. Despite the greater warming over the ocean in fall, the ensemble-mean warming over land is somewhat larger in summer compared to fall because of the mechanisms enhancing summertime warming over land discussed in Section 4.2. As with the WRF-CCSM4 seasonal warming pattern, a striking feature of the ensemble-mean seasonal warming pattern is the land-sea warming contrast in summertime in the coastal zone. It is significant that during this warmest season of the year, the warming is largest in the areas where temperatures are already greatest in the baseline climate. As we will discuss in Section 7, this has important consequences for increases in the frequency of extremely hot days. Enhanced warming at high elevations is apparent during summer and fall, and to a lesser degree, during spring.

The span of the 95% confidence interval for each season is shown in Fig. 14. This is a measure of the inter-model spread in the warming and the model-based uncertainty. Though substantial uncertainty is seen in all seasons, it is particularly large in fall (roughly 3°F to 3.5°F). This may be understood by referring to the large-scale controls on warming in the GCMs (Fig. 10). Examining Fig. 10b, the spread of land-sea warming contrast is larger in fall, ranging from almost no warming contrast, to one of nearly 3.5°F. When the statistical model regionalizes these wide variations, it likewise produces a variety of local warming predictions. The GCMs may exhibit such a large spread in the land-sea warming contrast because of fall's position as a transition season between winter and summer. Very large land-sea warming contrast is consistently seen in all GCMs in summer, and very little is consistently seen in winter, largely because of the dryness of the land surface in summer and its wetness in winter, as discussed in Section 4.3. Some GCMs exhibit a land-sea warming contrast in fall that is summer-like, while others exhibit one that is winter-like, depending on how each GCM simulates the seasonal increase in soil moisture going from summer to winter.

The uncertainty interval may be smallest in summertime partly because of the consistently large land-sea warming contrast seen in the GCMs (Fig. 10b) and also because the inter-model spread in the overall regional warming is relatively small during this season (Fig. 10a).

6.3 Local Warming

In this section, we briefly discuss the implications of the RCP8.5 annual-mean warming pattern and its uncertainty (Fig. 12, panels a, b, and c) for various locations within the region. Fig. 15 shows the annual-mean, ensemble-mean warming values and their uncertainty intervals for locations in the city of Los Angeles, Los Angeles County, and the Los Angeles region (red dots and associated bars). The values are also reported in Table 2. The locations are shown on maps in Fig. 16.

For most districts within the city of Los Angeles (Fig. 15a), the ensemble-mean warming is similar, around 4ºF, though the locations within the San Fernando Valley show slightly greater warming. Apparently, even the presence of the relatively low Santa Monica Mountains gives these locations a slightly more inland-like warming. The cities within Los Angeles County (Fig. 15b) are far enough apart that their warming begins to show the influence of the land-sea warming contrast seen in Fig. 12b to a greater degree. Within the coastal zone, the warming is very similar to that of the city of Los Angeles. However, for cities separated from the coast by a topographic barrier (Santa Clarita, Lancaster, and Palmdale), the warming is nearly 1ºF larger. For locations within the region outside of Los Angeles County (Fig. 15c), a similar pattern is seen. If the location is separated from the coast by a topographic barrier, its expected warming is larger. Desert and high elevation locations (Palm Springs, Wrightwood, and Big Bear Lake) show particularly large warming of 5ºF to 5.5ºF. Note that the variations in warming from location to location seen in Fig. 15 are somewhat enhanced in summertime (not shown), consistent with the larger land-sea warming contrast in this season (Fig. 13). The uncertainty ranges in Fig. 15—roughly ±2.5ºF to ±3ºF—are similar at all locations within the region.

7 Changes in Extreme Heat

So far we have quantified changes in the time-mean surface air temperature in the Los Angeles region. Next we explore the implications of these changes for extremely hot days. We define extremely hot days in two ways, one based the changes in the number of days with daily maximum temperatures exceeding a fixed threshold of 95°F, and another based on the number of days exceeding a geographically-varying threshold. This

geographically-varying threshold is based on the typical local temporal variation in temperature. The daily maximum surface air temperature is calculated as a combination of the model's skin temperature and 2-meter air temperature at 4pm local time, i.e., two-thirds of skin temperature values plus one-third of 2-meter air temperature values. The time 4pm is assumed as the time at which the daily maximum temperature is reached albeit not always true in observations. It is chosen because of the model's output frequency. This metrics to define the maximum temperature has been validated in comparison with the measurements in 21 observational sites in the Los Angeles region. And it has been demonstrated a very good proxy of the observed daily maximum surface air temperature.

Fig. 17 provides an illustration of how this calculation was done. The blue curves show the Probability Density Function (PDF) of daily maximum temperature in the baseline climate for all four seasons. Two representative sub-regions are chosen and analyzed separately, the coastal zone and land interior, for a total of eight cases. It is also possible to calculate temperature PDFs for the WRF-CCSM4 simulation in the future climate period. This involves a shift of the entire distribution to the right, since the climate warms (not shown). We find that the magnitude of the shift is almost identical to the mean warming, though there is also a slight change in the distribution's shape. It is not possible to directly calculate a maximum daily temperature PDF for the future regional climate states associated with the other GCMs. These models were not downscaled dynamically, and so the required temporal resolution is not available. Instead we use an indirect method. We assume that the maximum daily temperature PDF changes in the same way as in the WRF-CCSM4 simulation, except that the shift to the right from the baseline climate is given by the statistically-downscaled warming associated with the particular GCM in question. This gives a family of new PDFs associated with every GCM. The average of these PDFs corresponds to the ensemble-mean future PDF, and uncertainty can be inferred from the spread in the PDFs. The red curves in Fig. 17 show the ensemble-mean PDFs of daily maximum temperature for the future climate period for the same eight cases noted above. The grey-shaded area provides a measure of the intermodel spread.

Using this method, we produce daily-maximum temperature PDFs of the baseline climate at every grid point, and the corresponding PDFs for the future regional climate state associated with every GCM. We then use this information to calculate how frequently a temperature threshold is breached every year in current and future climate cases. As noted above, we focus on two ways of defining this temperature threshold. In the first way, we choose a fixed value of 95°F as the temperature threshold beyond which the daily maximum is considered extreme. Fig. 18 shows the number of days per year this threshold is exceeded in the baseline climate at the various locations in the city of Los Angeles, Los Angeles County, and the Los Angeles region (green dots). Also shown is the projected future number of days this threshold is breached for the RCP8.5 scenario (red dots correspond to the ensemble-mean and associated bars represent uncertainty). This information is also presented in Table 3.

By this definition, the number of extremely hot days per year increases dramatically at many locations. The effect is especially pronounced inland, at locations separated from the coast by at least one mountain complex. Examining some dramatic cases: the number of extremely hot days per year is projected to increase from 54 to 97±28 in San Fernando, from 55 to 96±24 in Lancaster, from 58 to 103±27 in Riverside, and from 135 to 160±17 in Palm Springs. In the baseline climate, these inland cities experience many days whose maximum temperatures are close enough to 95°F that they are pushed over this threshold when warming occurs. In contrast, it is rare for coastal cities like Venice, Santa Monica, Torrance, and Oxnard to have summertime highs close to 95°F, so the same increase in mean temperature results in a relatively small increase in days per year with maximum temperatures above 95°F. This contrast in behavior between coastal and inland locations is further exaggerated by the fact that the warming itself is larger in the inland locations, especially in summer (see Fig. 13d).

Choosing an absolute threshold to define heat extremes may have limited utility, since locations with many extremely hot days in the baseline climate may already be adapted to extremely hot weather. Therefore we also include an analysis where the threshold defining an extremely hot day varies geographically, according to the typical temperature variations seen in the baseline climate at the location in question. We choose

the 98th percentile of the daily maximum temperature PDF as the threshold. In other words, at any particular location, the threshold is defined so that roughly the seven hottest days per year will exceed it in the baseline climate. The values for this threshold at the various locations are shown in the first column of Table 4. Then we calculate how many days per year exceed this threshold in the future. Fig. 19 and the accompanying Table 4 show the results of this exercise. As in Fig. 18, the green dots show the number of days the threshold is exceeded in the baseline climate. (By design, this number is the same at all locations, roughly seven, as noted above.) Examining the results corresponding to the RCP8.5 scenario (red dots and associated bars), the most likely change in the number of extremely hot days ranges from a doubling or tripling near the coast to a quintupling or sextupling at inland locations. Thus even after taking into account the fact that the baseline climate is cooler near the coast, the coastal locations still experience smaller increases in extremely hot days. Even within the relatively small area corresponding to the City of Los Angeles, the effect is apparent. Near the coast and south of the Santa Monica Mountains, the number of extremely hot days approximately triples, while in the San Fernando Valley, roughly four times as many extremely hot days are seen. The effect is even more dramatic when locations within the county and the region are considered. Thus the summertime land-sea warming contrast seen in Fig. 13d has a significant impact on the geographical distribution of heat extremes in the future climate, no matter how they are defined.

8 Sensitivity to Choice of Emissions Scenario

As discussed in Section 2, the evolution of globally-averaged surface air temperature over the 21st century is dependent not only of the choice of GCM, but also on the emissions scenario (Fig. 1c). In this section, we compare the warming outcomes when the GCM results of the RCP2.6 emissions scenario are regionalized to those associated with the RCP8.5 scenario. We regionalize the GCM responses to the RCP2.6 scenario, including that of CCSM4, using the same statistical model discussed in Section 5.1 and the Appendix.

Fig. 12e shows the resulting ensemble-mean warming pattern associated with the RCP2.6 scenario. The lower and upper bounds of the warming, based on a 95%

confidence interval, are also shown in Figs. 12d and f for the sake of completeness. We find that the expected warming under RCP2.6 has a similar pattern to that of RCP8.5, and is about 70% as large on a regionally-averaged basis (land only). The same information from a different vantage point is seen in Fig. 15, which provides the local perspective under the RCP2.6 scenario (yellow dots). At individual locations, the warming under RCP2.6 is also about 70% as large as that under RCP8.5. This figure also highlights the substantial overlap in warming outcomes between the two scenarios, as measured by the model uncertainty in expected warming. All these conclusions are roughly consistent with the global warming outcomes of the two scenarios (Fig. 1c). We also examine the change in extremely hot days under the RCP2.6 in Figs. 18 and 19 at various locations. For those locations showing a substantial increase in extremely hot days under RCP8.5, there is a noticeable increase under RCP2.6, though it is typically about half to two-thirds as large. As with the expected warming projections, the model uncertainty estimates of heat extremes for the two scenarios overlap to a large degree.

While near-term reductions in greenhouse gas emissions will likely mitigate anthropogenic warming in the Los Angeles region somewhat, the warming outcomes associated with the two scenarios seem more similar than different. The majority of the warming seen in the more aggressive emissions scenario would still occur by mid-century at all locations under RCP2.6, and heat extremes at inland locations would still increase noticeably. Therefore adaptation to a changing climate in the region is likely to be inevitable.

9 Summary and Discussion

Using a combination of dynamical and statistical downscaling techniques, we projected mid-21st century warming in the Los Angeles region at 2-km (1.2-mile) resolution. Computationally-intensive dynamical techniques were used to downscale a climate change simulation done with a single global climate model (CCSM4). Then a statistical model was developed to reproduce the downscaled temperature response of the dynamical model, given information from the global model. The statistical model was then used to downscale other global climate simulations.

To account for uncertainty associated with the trajectory of future greenhouse gas emissions and other factors affecting the planet's energy balance, we examined projections for both "business-as-usual" (RCP8.5) and "mitigation" (RCP2.6) emissions scenarios of the Fifth Coupled Model Intercomparison Project (CMIP5). Under the business-as-usual scenario, greenhouse gas emissions continue to increase at comparable rates to those of the past decade, while under the mitigation scenario, emissions begin to decline over the next few decades, consistent with a global effort to control emissions in the near future. We view these two scenarios as estimates of the maximum and minimum greenhouse gas emissions over the coming century. To account for uncertainty associated with choice of global climate model, we downscaled results for all available global models in the CMIP5 archive. This amounts to roughly 20 climate models.

For the business-as-usual scenario, we find that by the mid-21st century, the most likely warming is roughly 4.6°F averaged over the region's land areas. High elevations and inland areas separated from the coast by at least one mountain complex warm 20 to 50% more than the areas near the coast or within the Los Angeles basin. The differential warming is especially apparent in summertime. The summertime warming contrast between the inland and coastal zones has a large effect on the most likely expected number of extremely hot days per year. Coastal locations and areas within the Los Angeles basin see roughly two to three times the number of extremely hot days, while high elevations and inland areas typically experience approximately three to five times the number of extremely hot days. In the mitigation scenario, the most likely warming and increase in heat extremes are somewhat smaller. However, the majority of the warming seen in the business-as-usual scenario still occurs at all locations in the most likely warming under the mitigation scenario, and heat extremes still increase significantly. Because it is very unlikely that humans will emit less greenhouse gases than in the mitigation scenario, adaptation to a changing climate over the next few decades is probably inevitable in the Los Angeles region.

We wish to emphasize that the main conclusions reported here for each emission scenario are subject to large spatially-varying uncertainties due to the variety of warming responses seen in the current generation of global climate models and the

regionalization of those responses. For example, for a 95% confidence interval, the annual-mean warming at downtown Los Angeles under the business-as-usual scenario at mid-century ranges from 1.3 to 6.5°F. In other words, we believe there is a 19 out of 20 chance that the actual warming under business-as-usual would fall in this range. The uncertainty ranges are comparable for all other locations within the region, though they tend to increase going inland. The uncertainty in the average warming leads to a correspondingly large uncertainty in the changes in the number of extremely hot days. To take the example of downtown LA again, we project with 95% confidence that the number of days with a maximum temperature above 95°F will rise to between 10 and 48 days per year under business-as-usual (from a value in the baseline climate of about 5.6 days per year). These uncertainty ranges underscore the fact that the warming that actually materializes in the Los Angeles region by mid-century could be significantly less or more severe than the most likely outcomes reported here.

Since the mitigation and business-as-usual emission scenarios are extreme cases, the smallest possible warming under the mitigation scenario and the greatest possible warming under business-as-usual provide reliable estimates of the entire range of climate possibilities at any location, given current knowledge. To take again the example of downtown Los Angeles, the lower bound of the annual-mean warming under RCP2.6 is 0.6°F, while the upper bound under RCP8.5 is 6.5°F. Therefore, we anticipate with high confidence that the actual warming in downtown Los Angeles will be somewhere in this range, no matter what greenhouse gas emissions scenario unfolds between now and mid-century. Using this same simple method and the data provided in Tables 2,3, and 4, similar conclusions can be drawn for other locations.

Finally, we note that the baseline climate period against which the future climate state is compared to compute a climate change signal is not precisely the present-day at the time of publication of this study (2012). To the degree that the climate in the region has already changed since the baseline period due to anthropogenic forcing, the warming that materializes between 2012 and mid-century may be less than projected here. However, our choice of baseline period may still be most appropriate for policy

planning, since local infrastructure reflects an adaptation to environmental conditions at the time of construction, not the present.

Appendix

Here we provide a detailed description of the statistical model used for downscaling warming in the various GCMs.

As noted in Section 5.1, our statistical model requires three input parameters from the GCMs: (1) The overall regional warming, (2) the land-sea warming contrast, and (3) the lapse rate change. To calculate the land-sea warming contrast we need to sample the warming in each GCM over both inland and ocean regions. It is not obvious how to do this because each GCM has different resolution and thus different topography. Most GCMs do not have a representation of the mountain complexes that clearly separate the coastal regions from the desert. There is simply a gradual slope from the ocean up to the Sierra range. So to calculate dT^{inland}, the GCM-predicted warming over the inland area near the Los Angeles region, we average the warming over an inland region (116°W-119°W, 37°N-41°N), that is as close as possible to the coast, while still representing an inland location regardless of which GCM is used. There are similar problems with selecting an ocean region. The grid boxes for the GCMs are larger than the typical horizontal length scales of the coastal topography. Thus depending on the exact location and size of the coastal grid boxes in each GCM, each box may be representing a different mix of ocean, low-lying coastal land, and mountains. Thus we calculate dT^{ocean}, the GCM-predicted warming over the ocean off the coast of the Los Angeles region, by averaging the warming over an ocean region (118°W-120°W, 32°N-34°N), which accurately represents the coastal ocean in each GCM. The land-sea warming contrast is the difference between the average warming over the desert region minus the average warming over the ocean region, $\Delta_{coast} dT = dT^{inland} - dT^{ocean}$.

To compute the overall regional warming, we use the average of the desert and ocean regions, $\overline{dT} = (dT^{inland} + dT^{ocean})/2$. This is a more robust way to measure the overall warming than just taking the value of the warming at the GCM grid point(s) covering our domain. As mentioned above, the coastal zone is not well represented in GCMs because it is narrow compared to the width of a GCM grid box. So averaging the

warming over a grid box encompassing a coastal area is sensitive to how much ocean or land area it covers, which is dependent on GCM resolution and the location of the GCM grid box. Instead, we use the average of the warming over the inland and ocean regions, as specified above. With this approach, we are certain what surface type the GCMs represent in each of these two regions. Since our domain is approximately half ocean or low-lying coastal points and half desert or high-elevation points, the degree of marine or inland influence on the regional-mean temperature will be approximately correct.

To calculate the lapse rate change, we compute the GCM warming at each height over the region 116°W-126°W, 28°N-38°N. The output from the CMIP5 GCMs is archived at course vertical resolution. Most models have output at pressure levels 1000, 925, 850, 700, 600 hPa. Because of the coarse resolution, we must interpolate between the levels to calculate $dT_{GCM}(z)$ and $dT_{CCSM4}(z)$.

Now that we have discussed how to extract the regional-mean warming, the land-sea warming contrast, and the lapse rate change from a GCM, we give a detailed mathematical description of how the statistical model digests these numbers to estimate the high-resolution warming pattern. The statistically predicted warming pattern is the sum of the regional mean warming, the coastal-inland contrast, and a high elevation correction (shown in Figure 8). Mathematically,

$$dT_{stat}(x,y) = \left(\alpha + \overline{dT}_{GCM}\right) + \left(\frac{\Delta_{coast}dT_{GCM}}{\Delta_{coast}dT_{CCSM4}}\right)\left(\beta \cdot dT_{dyn}(x,y)\right) + dT_{hi-elev}(z(x,y)) \cdot 1_{z>z_0}, \quad (*)$$

where

$$dT_{hi-elev}(z) = \left(dT_{GCM}(z) - dT_{GCM}(z_0)\right) - \left(\frac{\Delta_{coast}dT_{GCM}}{\Delta_{coast}dT_{CCSM4}}\right)\left(dT_{CCSM4}(z) - dT_{CCSM4}(z_0)\right) \quad (**)$$

is the high elevation correction applied only to locations where $z > z_0$. α and β are constants that are fit using linear regression to minimize error between the statistical and dynamical patterns. The term α represents the discrepancy of the dynamically downscaled regional mean compared to the regional mean estimated from the GCM. β is a scaling factor that dictates the size of the coastal-inland pattern. Using our dynamically

downscaled output, we compute that α ranges between -0.10°C (summer) and 0.15°C (fall).In contrast, β varies little by season, ranging from 0.26 (winter) to 0.39 (spring).

We apply the high elevation correction, $dT_{hi\text{-}elev}(z)$, for locations with elevation above $z_0 = 1200$m. Below z_0, the warming sampled from the GCMs is strongly linked to the land-sea contrast. Thus the regional mean and the land-sea contrast are sufficient to calculate the warming at lower elevations. Above z_0, the land-sea contrast is less representative of the warming signal. The second term in (*) assumes a constant relationship between the lapse rate change at high elevations and the land-sea contrast, given by CCSM4. However, by comparing different models we see that some GCMs can have the same land-sea contrast as CCSM4, but different lapse rate warming at high elevations. So, we remove the warming at high elevations due to term two, and add in the warming at high elevations from the GCM, yielding (**).

We apply this statistical model to 18 CMIP5 GCMs to obtain an approximation of the warming pattern that would result if these GCMs were dynamically downscaled using WRF. Note that each season was treated independently, so the whole process was repeated four times. This ensures we reconstruct the seasonality of the warming signals, such as those seen in Fig. 7. We undertook additional dynamical downscaling experiments to confirm that the statistical model produces accurate results. For example, we dynamically downscaled year-long future climate time slices for the GFDL-CM3, MIROC-ESM-CHEM, and CNRM-CM5 global models and compared the warming patterns to those projected by the statistical model. On average, we found that the statistical model errors at any particular location in any particular model and season were less than 10%, demonstrating that the statistical model we constructed can reproduce the dynamically-downscaled patterns with a high degree of accuracy.

References:

Boé, J., A. Hall, and X. Qu, 2009: Deep ocean heat uptake as a major source of spread in transient climate change simulations. Geophys. Res. Lett., 36, L22701, DOI:10.1029/2009GL040845

Bony S. and Coauthors., 2006: How well do we understand climate change feedback processes? J. Climate, 19, 3445-3482.

Caldwell P., H.N.S. Chin, D.C. Bader, and G. Bala, 2009: Evaluation of a WRF dynamical downscaling simulation over California. Climatic Change, 95, 499-521.

Cayan D.R., 1996: Interannual climate variability and snowpack in the western United Sates, J. Climate, 9, 928-948.

Cayan, D.R., E.P. Maurer, M.D. Dettinger, M. Tyree and K. Hayhoe, 2008: Climate change scenarios for the California region. Climatic Change, 87, 21-42.

Chen, F., and J. Dudhia, 2001: Coupling an advanced land-surface/ hydrology model with the Penn State/ NCAR MM5 modeling system. Part I: Model description and implementation. Mon. Wea. Rev., 129, 569-585.

Chin H.S., 2008: Dynamical downscaling of GCM simulations: toward the improvement of fore- cast bias over California. LLNL-TR-407576, Lawrence Livermore National Lab. https:// e-reports-int.llnl.gov/pdf/365755.pdf, 16pp

Conil S., and A. Hall, 2006: Local regimes of atmospheric variability: A case study of Southern California. J. Climate, 19, 4308-4325.

Dudhia, J., 1989: Numerical study of convection observed during the winter monsoon experiment using a mesoscale two-dimensional model, J. Atmos. Sci., 46, 3077-3107.

Gent, P. R., and Coauthors, 2011: The Community Climate System Model version 4. J. Climate, 24, 4973-4991.

Giorgi, F., B. Hewitson, J. Christensen, M. Hulme, H. von Storch, P.Whetton, R. Jones, L. Mearns and C. Fu, 2001: Regional climate information - evaluation and projections. In: J.T. Houghton, Y. Ding, D.J. Griggs, M. Noguer, P.J. van der Linden, X. Dai, K. Maskell and C.A. Johnson (eds.). pp. 583-638. Climate Change 2001: The Scientific Basis. Contribution of Working Group I to the Third Assessment Report of the Intergovernmental Panel on Climate Change. Cambridge University Press.

Hall A., X. Qu, and D. Neelin, 2008: Improving predictions of summer climate change in the United States. Geophys. Res. Lett., 35, L01702, DOI:10.1029/2007GL032012

Held I.M. and Soden B.J., 2000: Water vapor feedback and global warming. Annu. Rev. Energy Environ., 25, 441-75.

Hughes M. , A. Hall, and R.G. Fovell, 2007: Dynamical controls on the diurnal cycle of temperature in complex topography. Clim. Dynam., 29, 277-292, DOI: 10.1007/s00382-007-0239-8

Hughes M. , A. Hall, and R.G. Fovell, 2009: Blocking in areas of complex topography, and its influence on rainfall distribution. J. Atmos. Sci., 66, 508-518, DOI: 10.1175/2008JAS2689.1

Hong, S.-Y., and Y. Noh, and J. Dudhia, 2006: A new vertical diffusion package with an explicit treatment of entrainment processes. Mon. Wea. Rev., 134, 2318-2341.

Kain, J. S., 2004: The Kain-Fritsch convective parameterization: An update. J. Appl. Meteor., 43, 170-181.

Lin, Y.-L., R. D. Farley, and H. D. Orville, 1983: Bulk parameterization of the snow field in a cloud model. J. Appl. Meteor., 22, 1065-1092.

Leung L.R., and S.J. Ghan, 1999: Pacific Northwest Sensitivity Simulated by a Regional Climate Model Driven by a GCM. Part II: 2XCO2 Simulations, J. Climate, 12, 2031-2053.

Leung L.R., Y. Qian , and X. Bian, 2003: Hydroclimate of the western United States based on observations and regional climate simulations of 1981-2000. Part I: seasonal statistics. J. Climate, 16, 1892-1911.

Lundquist, J.D., D.R. Cayan, 2007: Surface temperature patterns in complex terrain: Daily variations and long-term change in the central Sirra Nevada, California. J. Geophys. Res., 112, D11124

Manabe, S., Wetherald, R. T., and Stouffer, R. J., 1981: Summer dryness due to an increase of atmospheric CO2 concentration. Climatic Change, 3, 347-386.

Meehl, G.A., et al. ,2007: Global climate projections. In Climate Change 2007: The Physical Science Basis. Contribution of Working Group I to the Fourth Assessment Report of the Intergovernmental Panel on Climate Change [Solomon, S., D. Qin, M. Manning, Z. Chen, M. Marquis, K.B. Averyt, M. Tignor and H.L. Miller (eds.)] Cambridge University Press, Cambridge, United Kingdom, and New York, NY, USA.

Meinshausen, M., S. J. Smith, K. V. Calvin, J. S. Daniel, M. Kainuma, J.-F. Lamarque, K. Matsumoto, S. A. Montzka, S. C. B. Raper, K. Riahi, A. M. Thomson, G. J. M. Velders and D. van Vuuren, 2011: The RCP Greenhouse Gas Concentrations and their Extension from 1765 to 2300. Climatic Change (Special Issue), DOI:10.1007/s10584-011-0156-z

Mlawer, E. J., S. J. Taubman, P. D. Brown, M. J. Iacono, and S. A. Clough, 1997: Radiative transfer for inhomogeneous atmosphere: RRTM, a validated correlated-k model for the long-wave, J. Geophys. Res., 102 (D14), 16663-16682.

Moss R., M. Babiker, S. Brinkman, E. Calvo, T.R. Carter, J. Edmonds, I. Elgizouli, S. Emori, L. Erda, K. Hibbard, R. Jones, M. Kainuma, J. Kelleher, J.-F. Lamarque, M.R.

Manning, B. Matthews, J. Meehl, L. Meyer, J.F.B. Mitchell, N. Nakicenovic, B. O'Neill, R. Pichs, K. Riahi, S.K. Rose, P. Runci, R.J. Stouffer, D.P. van Vuuren, J.P. Weyant , T.J. Wilbanks, J.P. van Ypersele, and M. Zurek, 2008: Towards new scenarios for analysis of emissions, climate change, impacts, and response strategies: IPCC Expert Meeting Report, 19-21 September 2007. Noordwijkerhout, The Netherlands, pp 155

Pan, L.-L., S.-H. Chen, D. Cayan, M.-Y. Lin, Q. Hart, M.-H. Zhang, Y. Liu, and J. Wang, 2011: Influences of climate change on California and Nevada regions revealed by a high-resolution dynamical downscaling study. Clim. Dynam., 37, 2005-2020.

Qian, Y., S.J. Ghan, and L.R. Leung, 2009: Downscaling hydroclimatic changes over the Western U.S. Based on CAM subgrid scheme and WRF regional climate simulations, Int. J. Climatol., 30: 675-693.

Skamarock W. C., J. B. Klemp, J. Dudhia, D. O. Gill, D. M. Barker, M. G. Duda, X.-Y. Huang, W. Wang, and J. G. Powers, 2008: A description of the Advanced Research WRF Version 3. NCAR Tech. Note NCAR/TN-475+STR, June 2008, 125 pp.

Sutton R.T., B. Dong and J.M. Gregory, 2007: Land/sea warming ratio in response to climate change: IPCC AR4 model results and comparison with observations. Geophys. Res. Lett., 34, L02701, doi:10.1029/2006GL028164

Solomon, S., D. Qin, M. Manning, Z. Chen, M. Marquis, K.B. Averyt, M.Tignor and H.L. Miller (eds.), 2007; Climate Change 2007: The Physical Science Basis. Contribution of Working Group I to the Fourth Assessment Report of the Intergovernmental Panel on Climate Change, Cambridge University Press, Cambridge, United Kingdom and New York, NY, USA.

Taylor K., R.J. Stouffer, and G.A. Meehl, 2009: A summary of the CMIP5 Experiment Design. http:// cmip-pcmdi.llnl.gov/cmip5/docs/Taylor_CMIP5_design.pdf

U.S. Metro Economies -- Gross Metropolitan Product with Housing Update, 2007: The United States Conference of Mayors and The Council for the New American City. Global Insight, Inc.

von Storch, H., E. Zorita and U. Cubasch, 1993: Downscaling of global climate change estimates to regional scales: An application to Iberian rainfall in wintertime. J. Climate, 6, 1161-1171.

Wang Y., L.R. Leung, J.L. McGregor, D.K. Lee, W.C. Wang, Y. Ding , and F. Kimura, 2004: Regional climate modeling: progress, challenges, and prospects. J. Meteor. Soc. Japan., 82, 1599-1628.

Wilby, R.L., S.P. Charles, E. Zorita, B. Timbal, P. Whetton, L.O. Mearns, 2004: Guidelines for use of climate scenarios developed from statistical downscaling methods: supporting material of the Intergovernmental Panel on Climate Change, Task Group on Data and Scenario Support for Impacts and Climate Analysis, Rotherham.

Winton, M., K. Takahashi, and I.M. Held, 2010: Importance of ocean heat uptake efficacy to transient climate change. J. Climate, 23, 2333-2344.
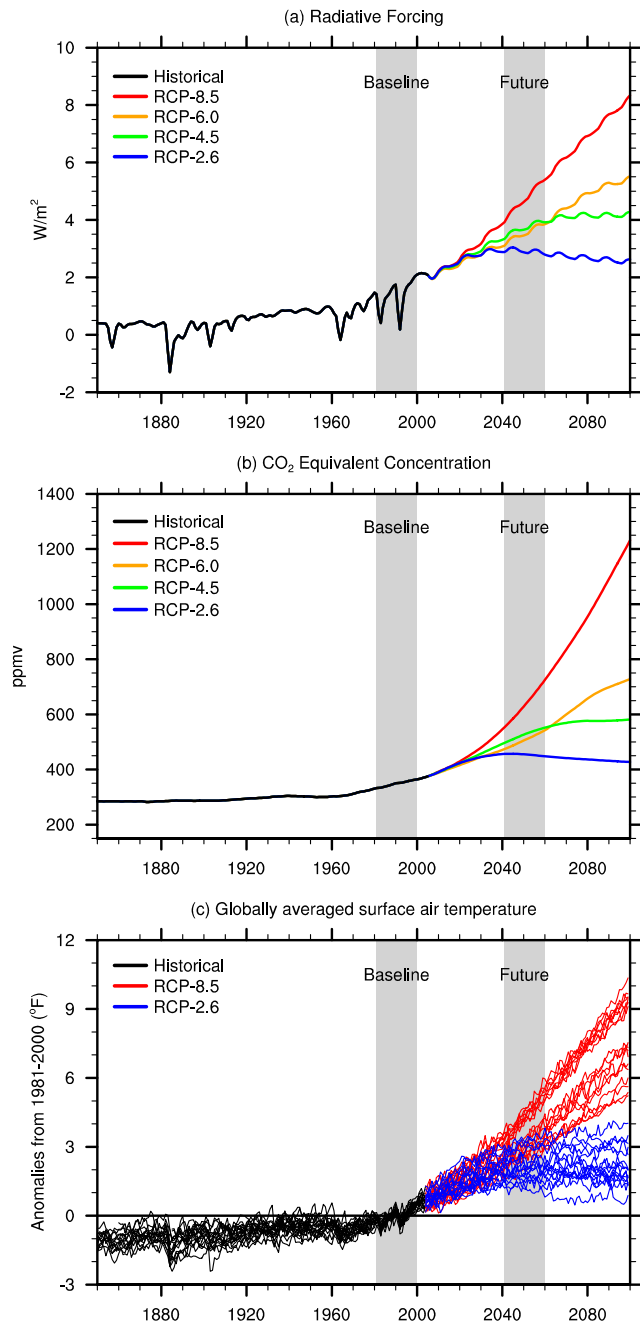
Figures:

Fig. 1: (a) Total radiative forcing (anthropogenic plus natural) and (b) Carbon dioxide (CO_2) equivalent concentrations for approximately the past century and four Representative Concentration Pathways: RCP8.5, RCP6, RCP4.5 and RCP2.6 (also called RCP3-PD); (c) Global-mean surface air temperature departures from 1981-2000 mean as simulated in all AR5 GCMs used in this study for the historical forcing (black), and RCP8.5 (red) and RCP2.6 (blue). Grey shaded regions denote the baseline (1981-2000) and future (2041-2060) periods used in this study.
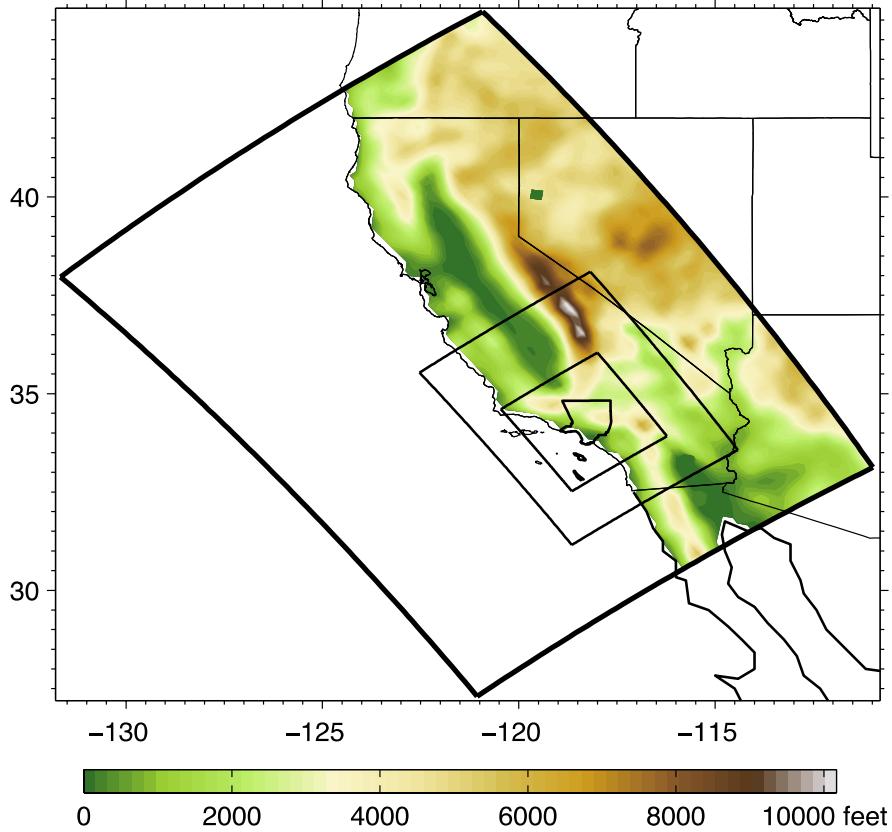
Fig. 2: WRF simulation domains at 18, 6 and 2km resolution (from the outermost to innermost grid). Elevation (unit: feet) is also shown in color, but at the resolution of the outermost domain. The innermost domain (2km resolution) is used in this study, where Los Angeles County is outlined. Coarse-resolution atmospheric forcings are applied to the boundary of the outermost domain. The baseline period (1981-2000) is forced using NARR data, while the future (2041-2060) period is forced using NARR data perturbed by the CCSM4 RCP8.5 scenario run.
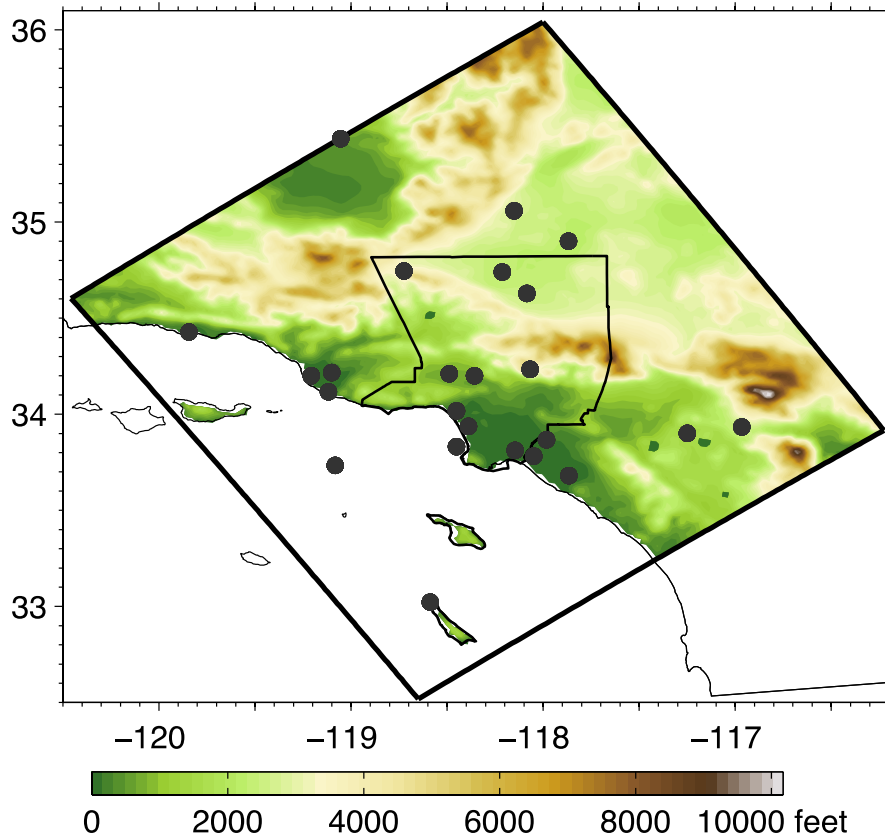
Fig. 3: Topography of the innermost domain, shown in color at the domain's 2km resolution. The border of Los Angeles County is also shown. Black dots represent point measurement sites from which observations are used to validate our dynamically downscaled baseline climate simulation.

Baseline Surface Air Temperature

(a) Fall (SON)

(b) Winter (DJF)

(c) Spring (MAM)
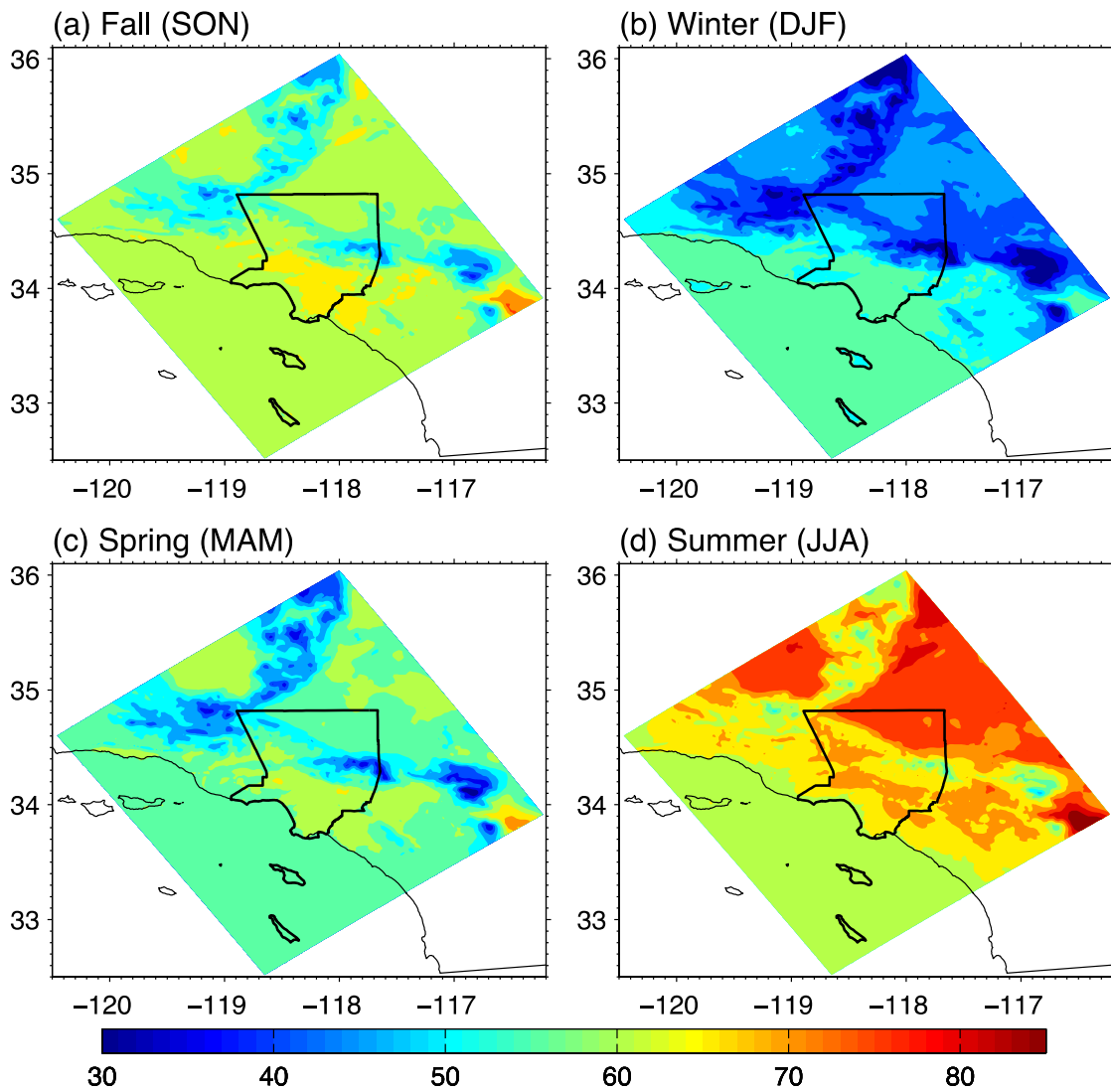

(d) Summer (JJA)

Fig. 4: WRF dynamically-downscaled seasonal-mean average surface air temperature (unit: °F) for the baseline period (1981-2000).
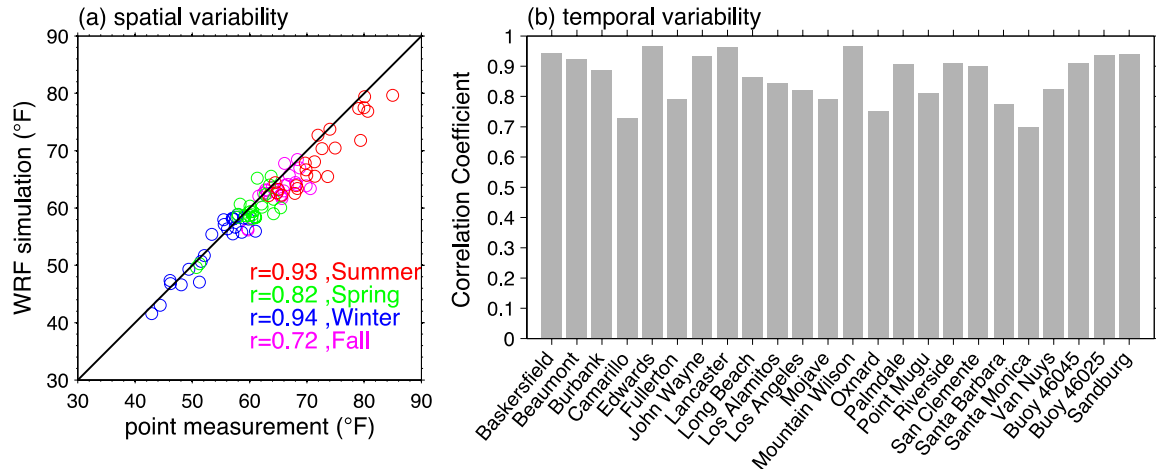
Fig. 5: (a) Validation of spatial variability of surface air temperature in WRF. This panel shows a comparison of the average seasonal-mean temperature observed at a point measurement site to the seasonal temperature simulated at the nearest grid point in the WRF domain for twenty-four point measurement sites. Points are color-coded by season. Observed temperatures are highly-correlated with simulated temperatures in each season. (b) Validation of temporal variability of surface air temperature in WRF. This panel shows correlation coefficients between observed monthly-mean temperature and simulated monthly-mean temperature for each of the twenty-four point measurement sites and the nearest model grid point. A climatological seasonal cycle was removed prior to calculation of a correlation. High correlation coefficients indicate that intermonthly and interannual variability in temperature is simulated realistically by the WRF framework.
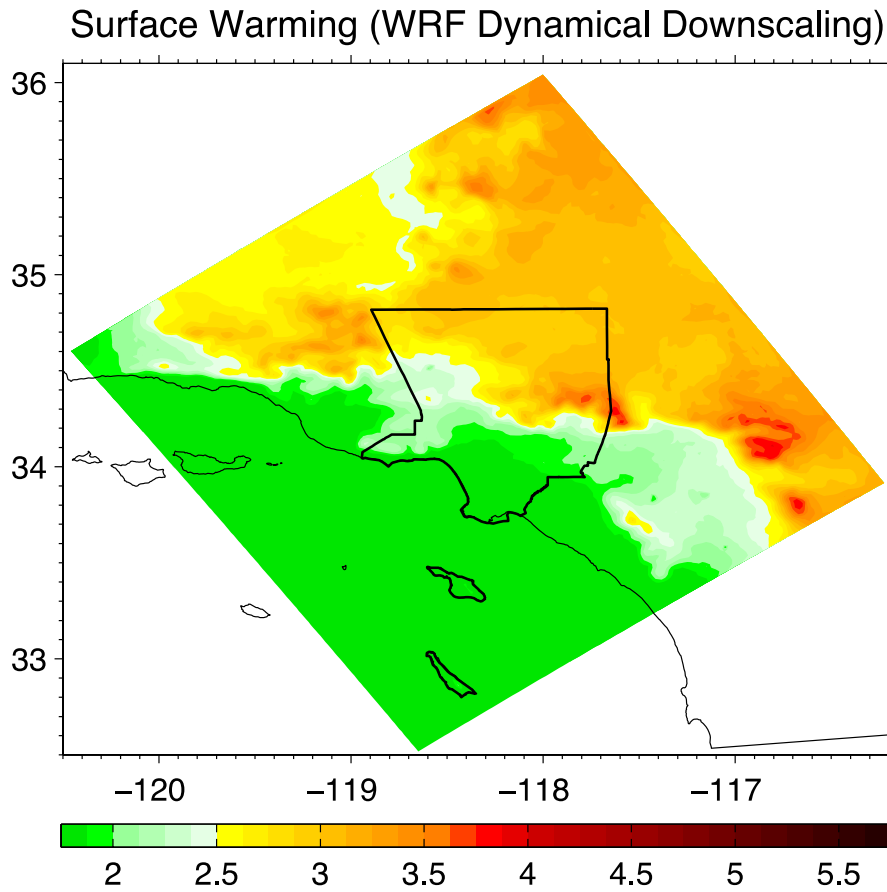
Fig. 6: WRF-CCSM4 dynamically downscaled annual mean surface air temperature change (future minus baseline), unit: °F. Note the contrast between inland and coastal warming, and stronger warming at higher elevations.
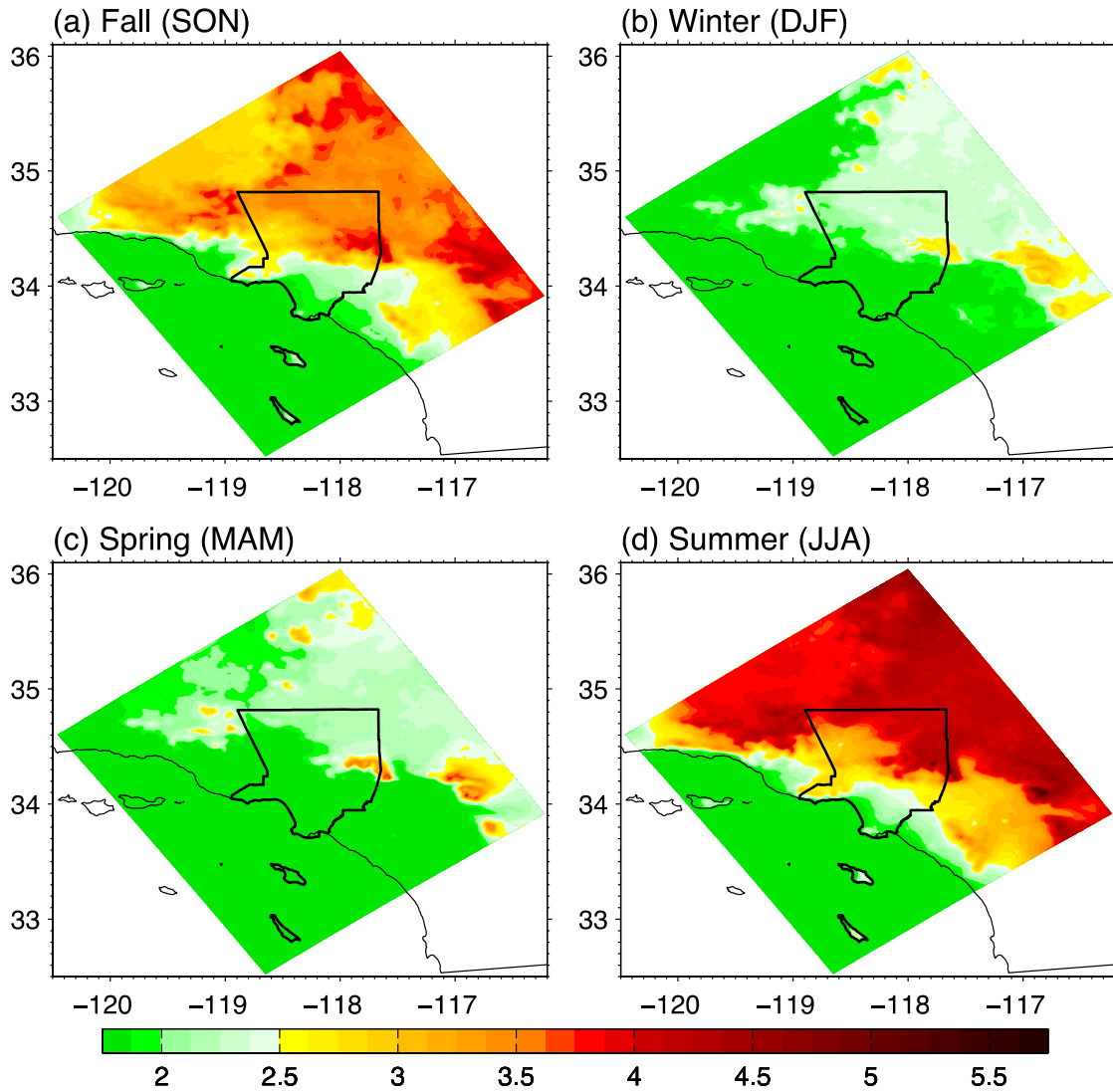
Fig. 7: WRF-CCSM4 dynamically downscaled seasonal-mean surface air temperature change (future minus baseline), unit: °F. Note the strongest warming in the summer months (JJA) over the desert interior, and also pronounced warming in the fall months (SON).
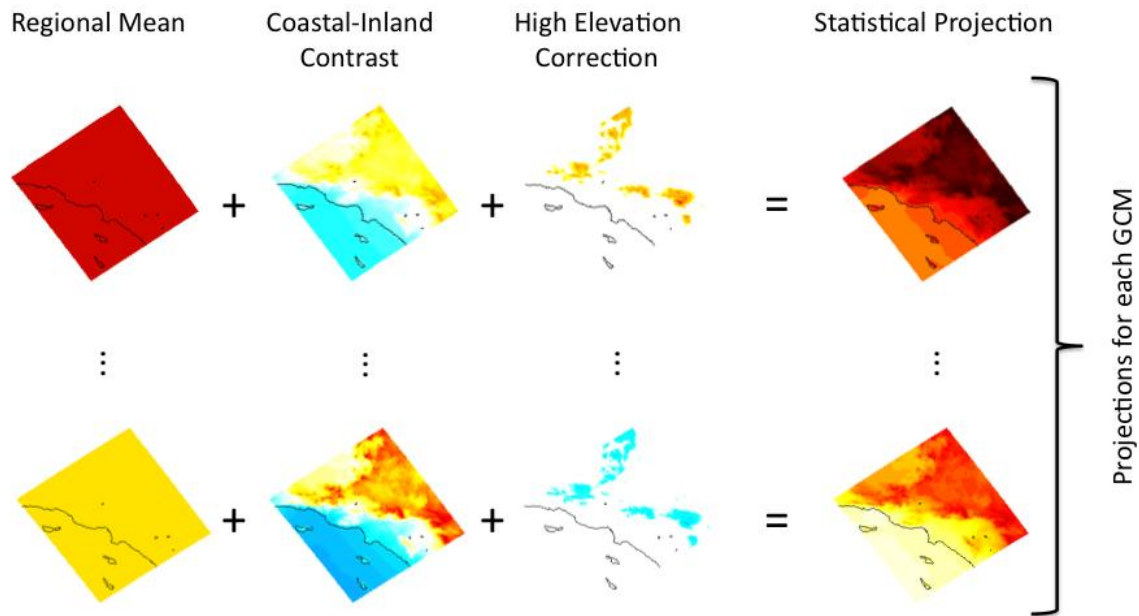
Fig. 8: Diagram of the statistical downscaling model methodology. The statistical downscaling model has three parameters: the domain-averaged warming, the warming contrast between desert and coastal and high elevation correction. The diagram illustrates how the spatial patterns corresponding to the three parameters are combined to produce the final statistically-downscaled projection for each model. Details of the statistical model are presented in the Appendix.
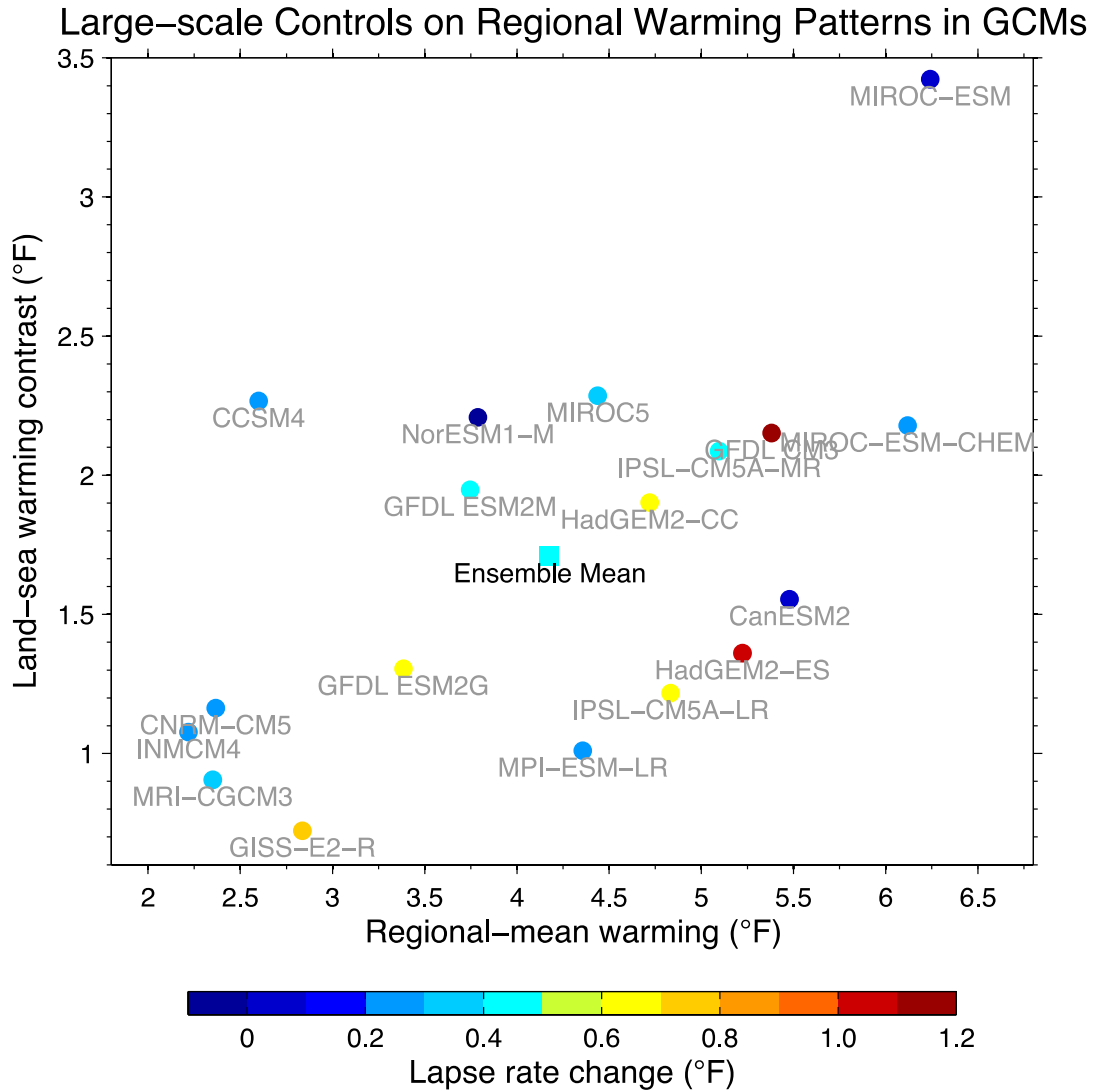
Fig. 9: Scatter plot of the annual mean variations of the two parameters used in our statistical downscaling model for each GCM: annual mean regional-mean warming vs. annual-mean land-sea warming contrast, color-coded by the value of the third parameter: the annual-mean change in the lapse rate over the North Pacific adjacent to the California coast. The square represents the average parameters for the entire ensemble (ensemble mean). The lapse rate change is defined as the warming at the altitudes corresponding to the highest elevations compared to the warming at the top of the main part of the atmospheric boundary layer. Further information about the definition of these parameters is given in the Appendix.

Fig. 10: Seasonal variations of the three parameters used in our statistical downscaling model for each GCM: (a) Regional-mean warming; (b) Land-sea warming contrast and (c) Lapse rate change, unit: °F. The green point represents the parameters for CCSM4, while the red point represents the ensemble mean. The lapse rate change is defined as the warming at the altitudes corresponding to the highest elevations compared to the warming at the top of the main part of the atmospheric boundary layer. Further information about the definition of these parameters is given in the Appendix.
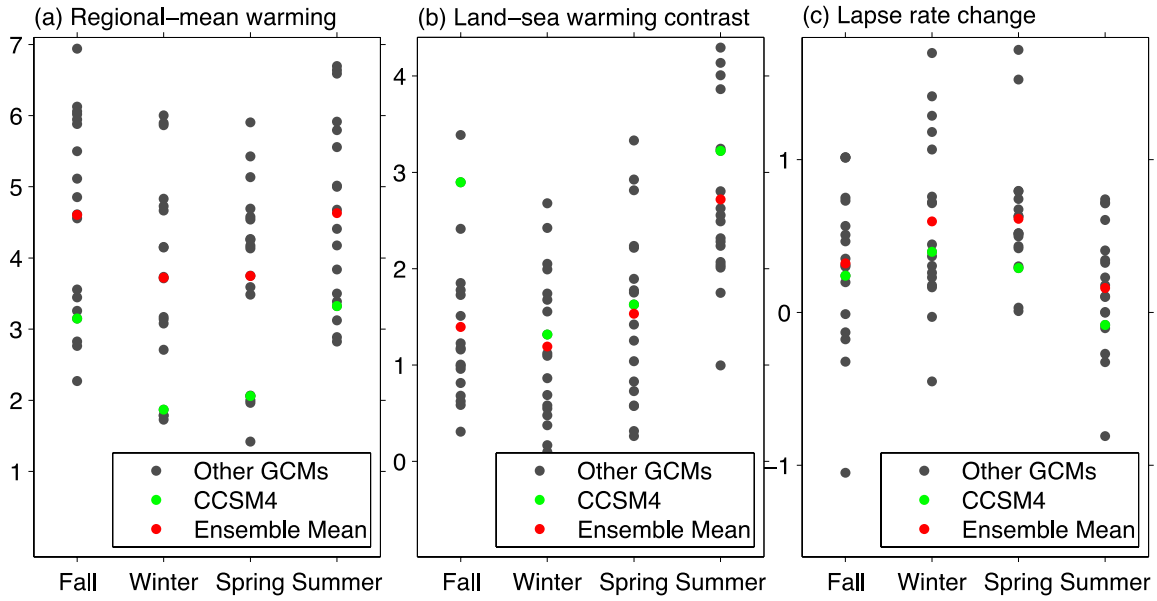
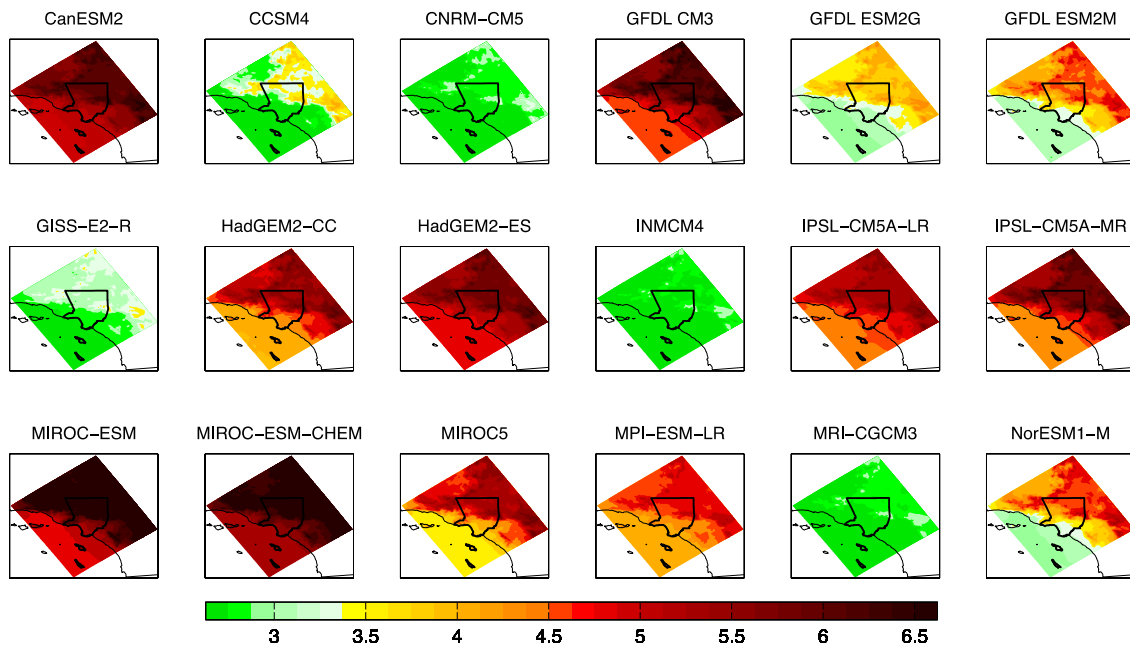## Surface Warming (Statistical Downscaling)

Fig. 11: Statistically downscaled results of annual mean surface air temperature change (future minus baseline) for each CMIP5 GCM, unit: °F.

Fig. 12: The ensemble-mean, annual-mean surface air temperature change (future minus baseline), and its uncertainty, unit: °F. Results from the RCP8.5 emissions scenario are show in the left panels, while those from the RCP2.6 emissions scenario are shown in the right panels. Panels (b) and (e) (the middle row) show the ensemble-mean, annual-mean surface air temperature change (future minus baseline) of all GCMs for the two emissions scenarios. The top row shows the lower bound of the 95% confidence interval of annual-mean surface air temperature change for all GCMS for RCP8.5 (a) and RCP2.6 (d), while the bottom row shows the upper bound of the 95% confidence interval of annual-mean surface air temperature change for all GCMS for RCP8.5 (c) and RCP2.6 (f).

Seasonality of Ensemble−Mean Surface Warming

Fig. 13: Ensemble-mean seasonal-mean surface air temperature change (future minus baseline) for the RCP8.5 emissions scenario (unit: °F).

Seasonality of 95% confidence interval
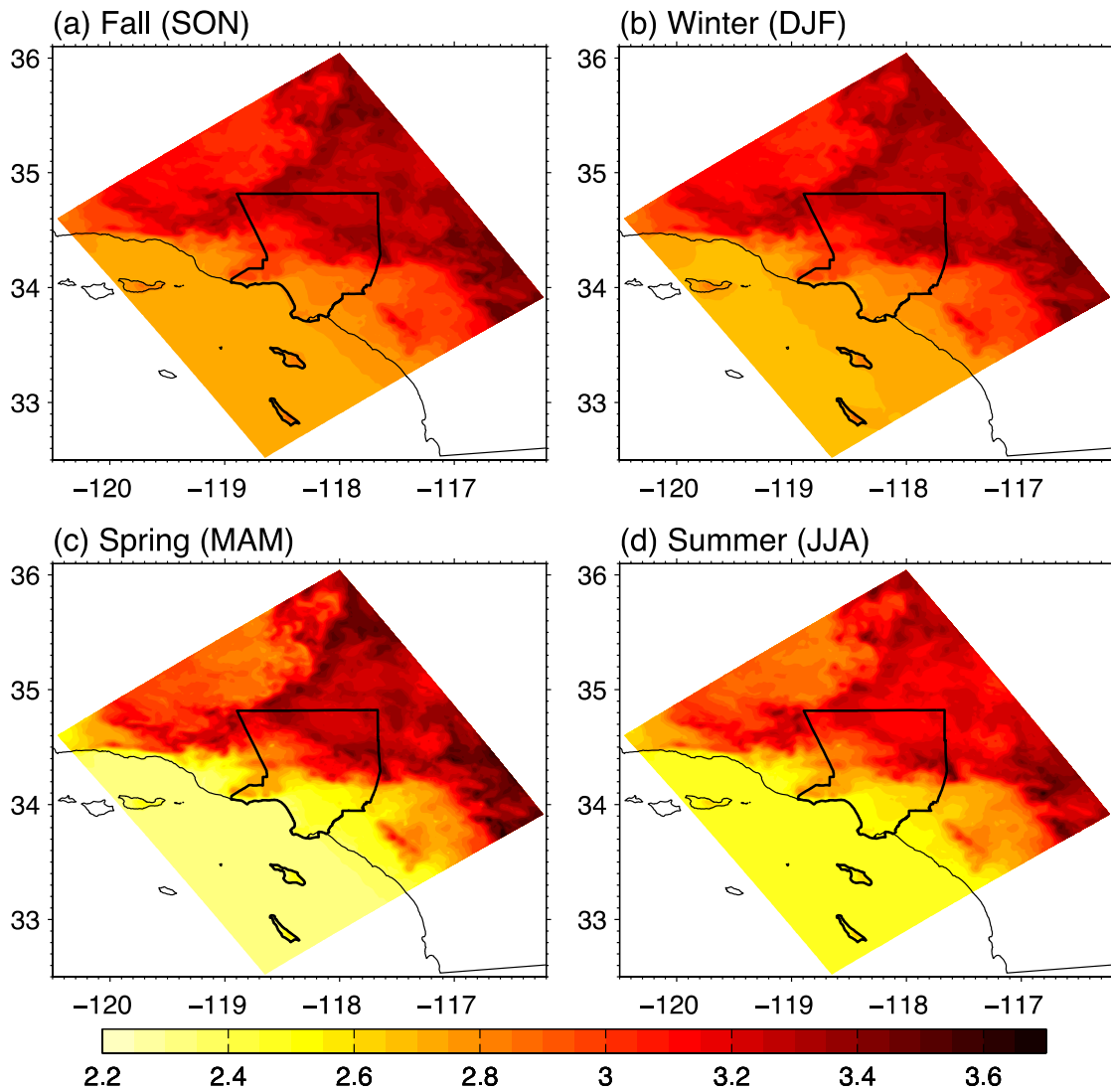
Fig. 14: The 95% confidence interval of the seasonal-mean surface air temperature change (future minus baseline, unit: °F) for the RCP8.5 emissions scenario. Uncertainty is generally largest in the fall and smallest in summer.
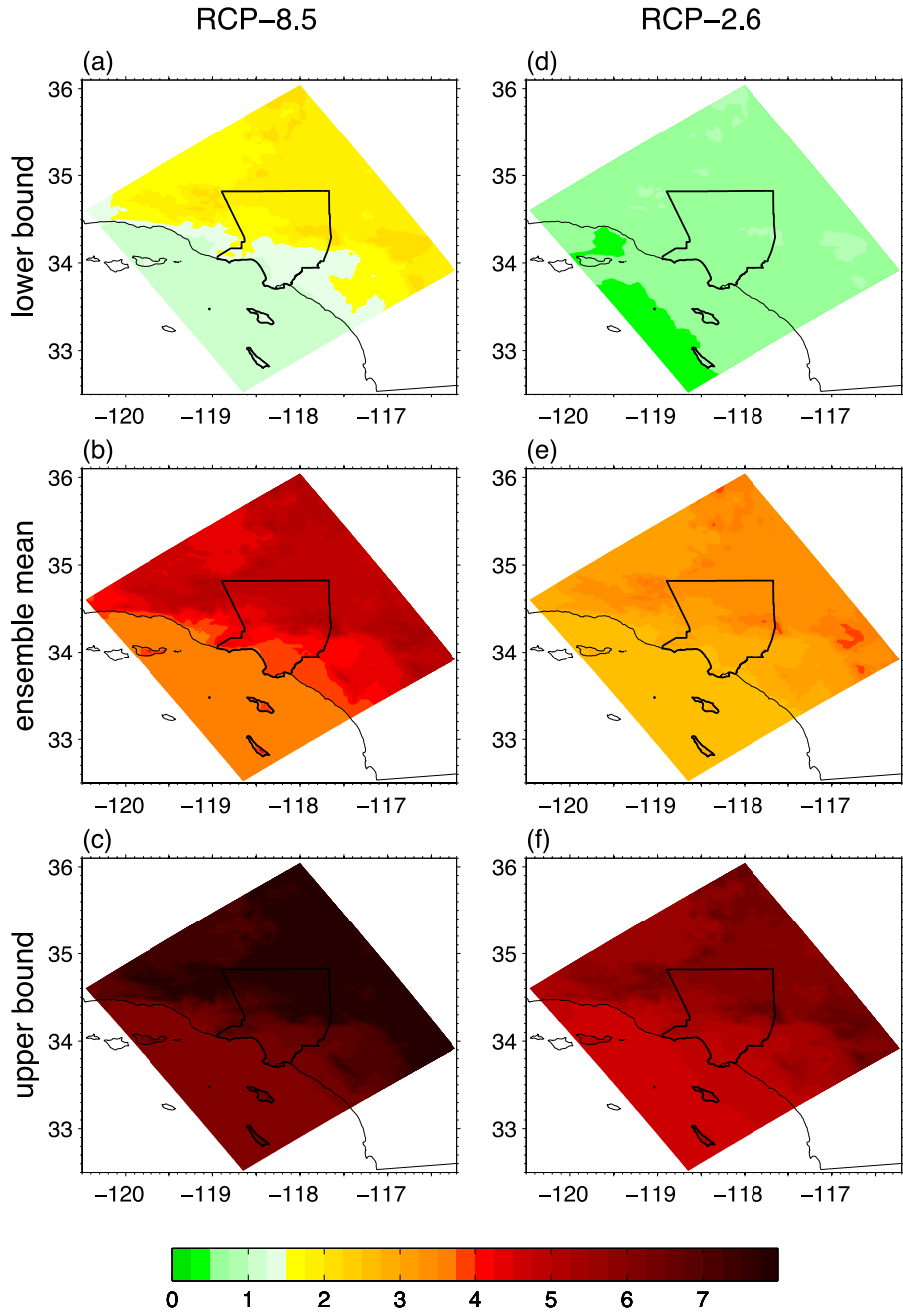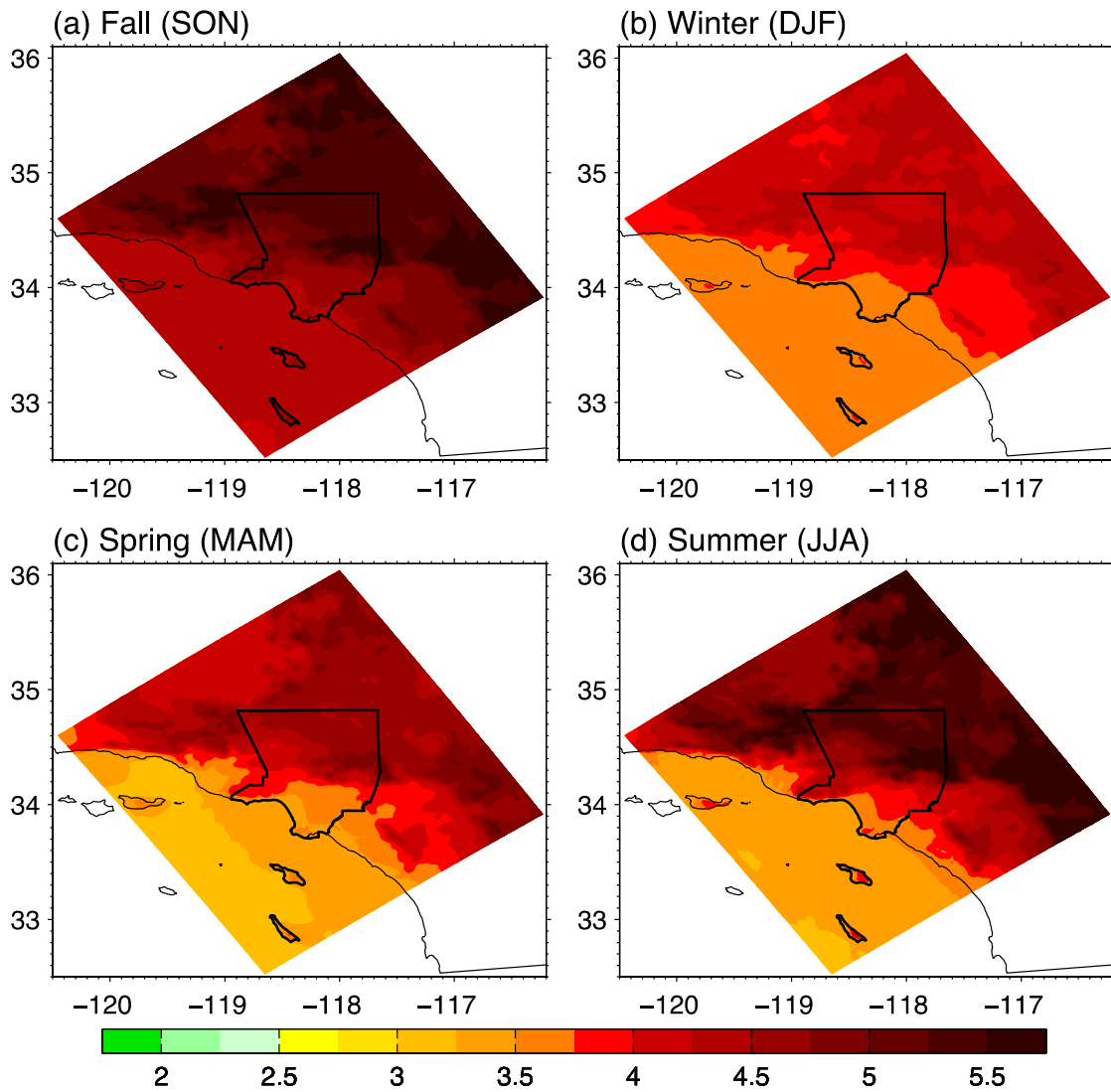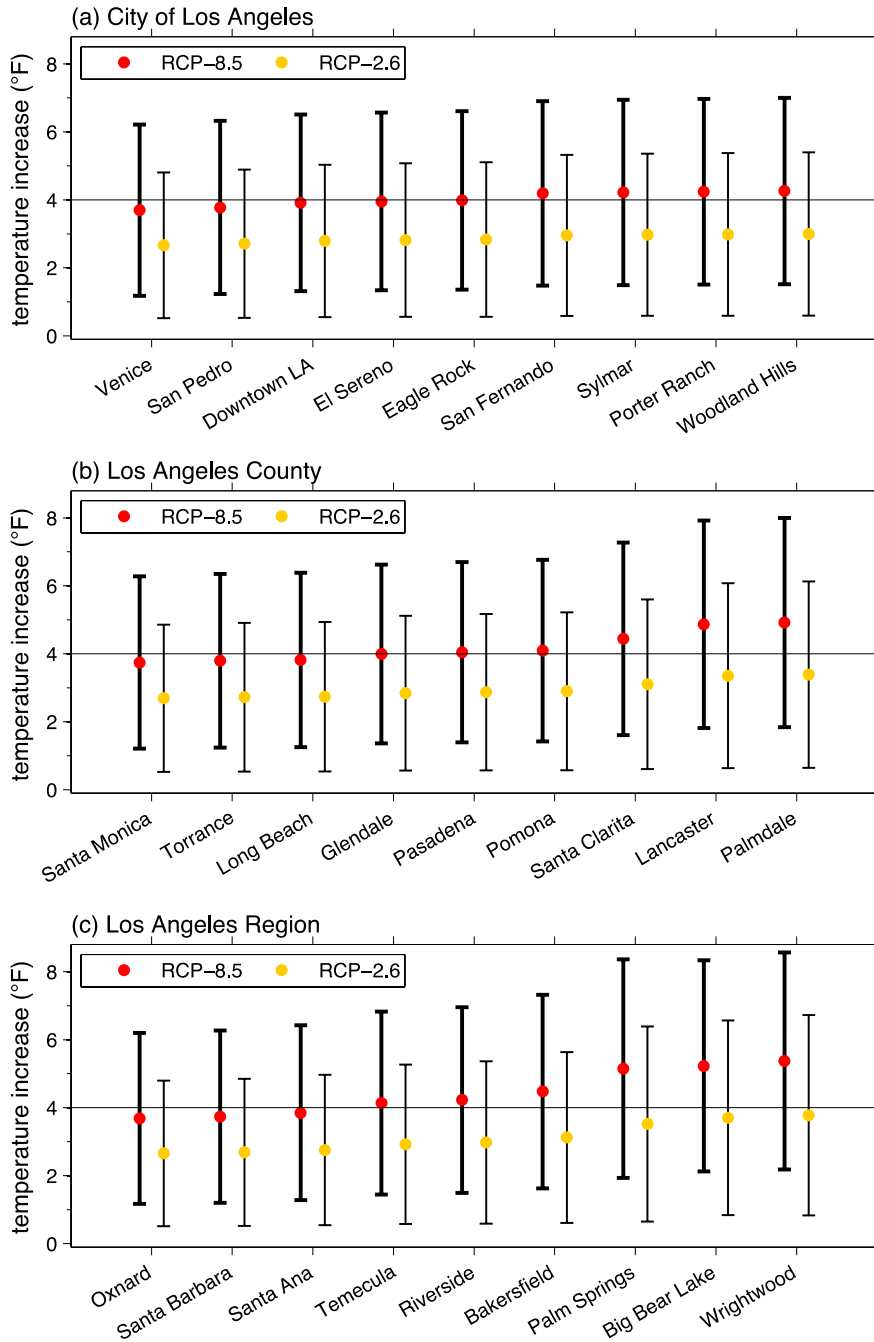
Fig. 15: The ensemble-mean annual-mean surface air temperature change (future minus baseline), and its uncertainty, for various locations. Results from both RCP8.5 (red) and RCP2.6 (yellow) emissions scenarios are shown. Panel (a) shows districts within the city of Los Angeles, panel (b) shows cities within Los Angeles County other than Los Angeles, while panel (c) shows cities within our study domain but outside of Los Angeles County. Dots represent the ensemble-mean, and whiskers represent the 95% confidence interval for the prediction, based on the spread seen in the regionalization of every available GCM. To aid the reader, a horizontal line corresponding to 4°F has been drawn on each panel.
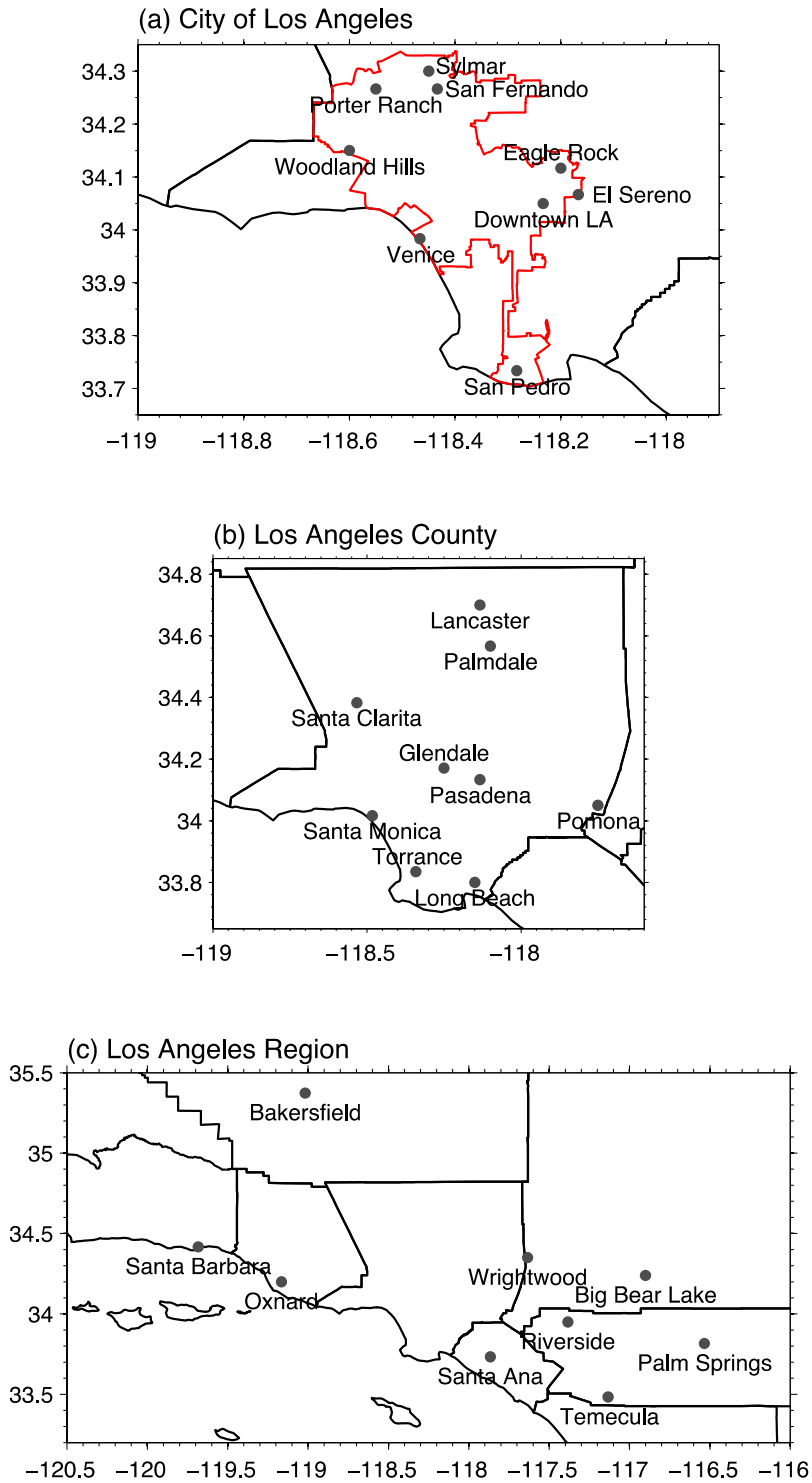
Fig. 16: Maps of locations in (a) the city of Los Angeles, (b) Los Angeles County, and (c) the Los Angeles region.
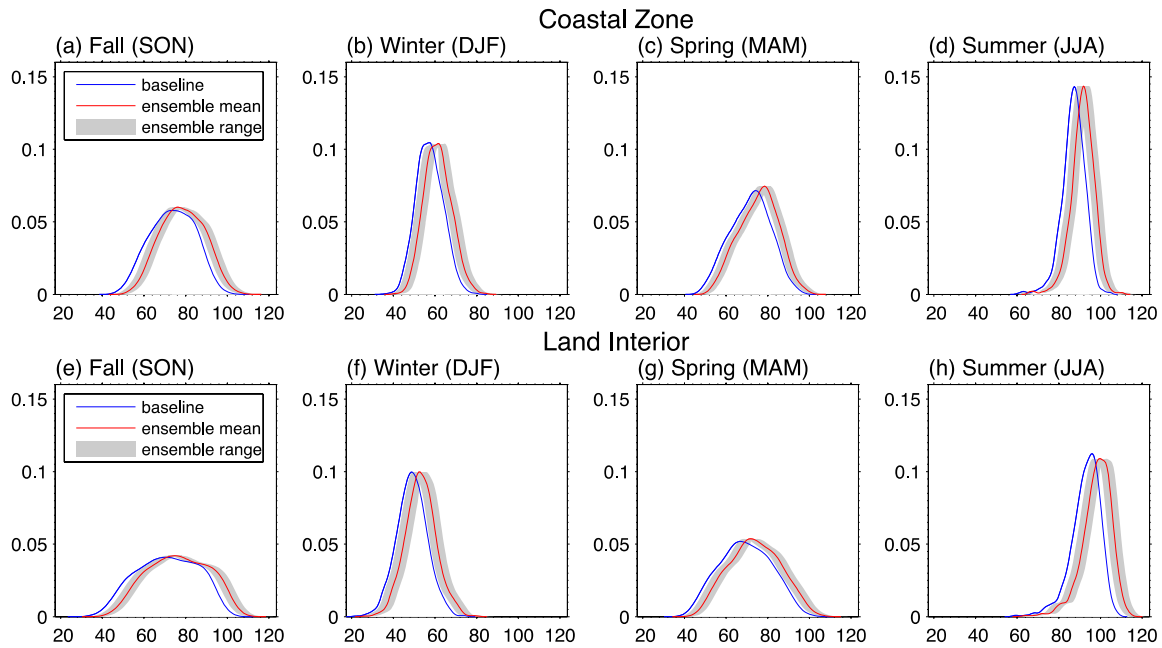
Fig. 17: Probability density functions (PDFs) of daily maximum surface air temperature averaged over coastal regions (upper) and inland regions (bottom) for each season, x-axis unit: °F. The coastal and inland regions are separated approximately by the summits of the main mountain complexes of Southern California. Temperatures are first area-averaged and then PDFs are calculated. The blue line represents the WRF dynamically downscaled baseline simulation (1981-2000). The red line represents the ensemble-mean shift in the distribution of surface air temperature in the future period (2041-2060) under the RCP8.5 emissions scenario. The associated 95% confidence intervals are shaded in gray.
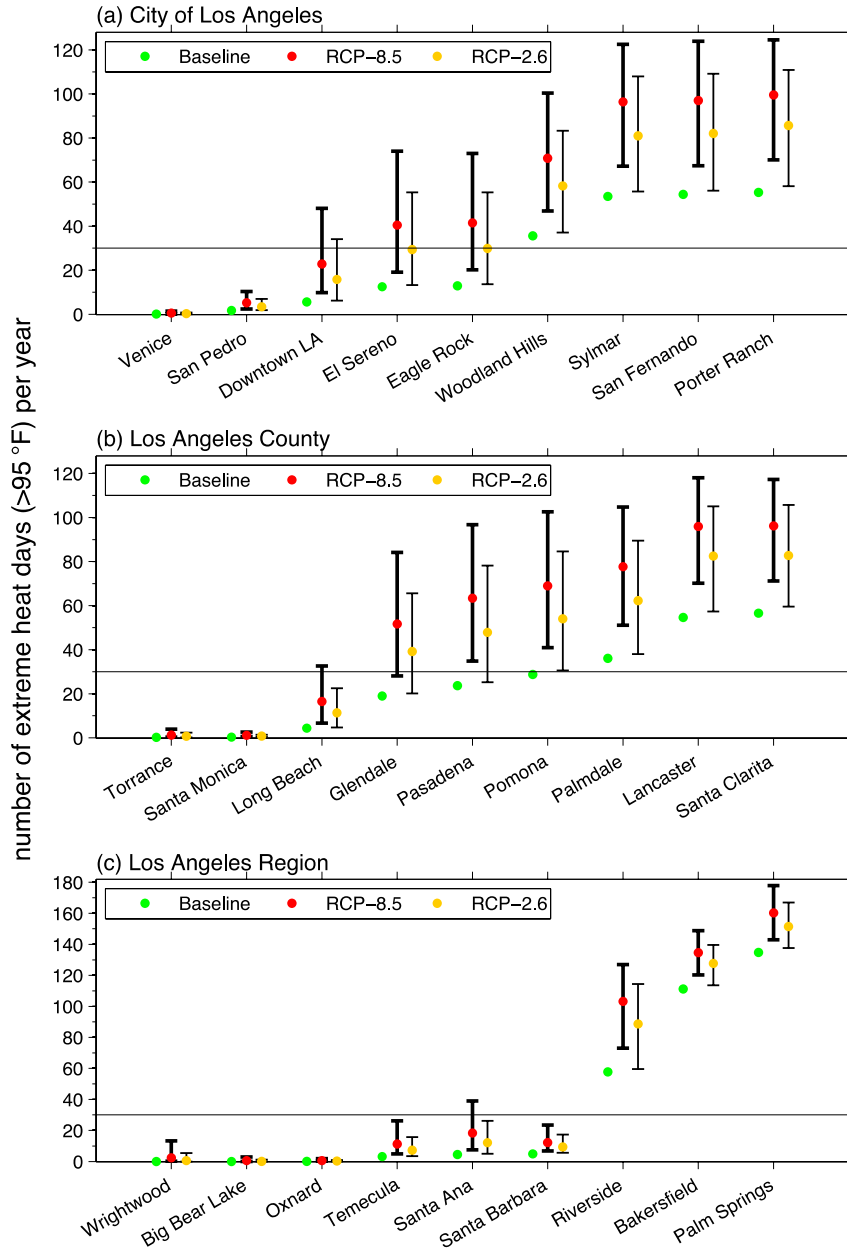
Fig. 18: The ensemble-mean annual-mean expected number of extremely hot days in the future period and its uncertainty, for various locations. The number of extremely hot days in the baseline period is shown with a green dot. An extremely hot day is defined as one where the maximum temperature is greater than 95°F. Panel (a) shows districts within the city of Los Angeles, panel (b) shows cities within Los Angeles County other than Los Angeles, while panel (c) shows cities within in our study domain but outside of Los Angeles County. Red and yellow dots represent the ensemble-mean for RCP8.5 and RCP2.6 emissions scenarios, respectively. Whiskers represent the approximate 95% confidence interval for the projection, based on the spread seen in the regionalization of every available GCM. To aid the reader, a horizontal line corresponding to 30 days per year has been drawn on each panel.
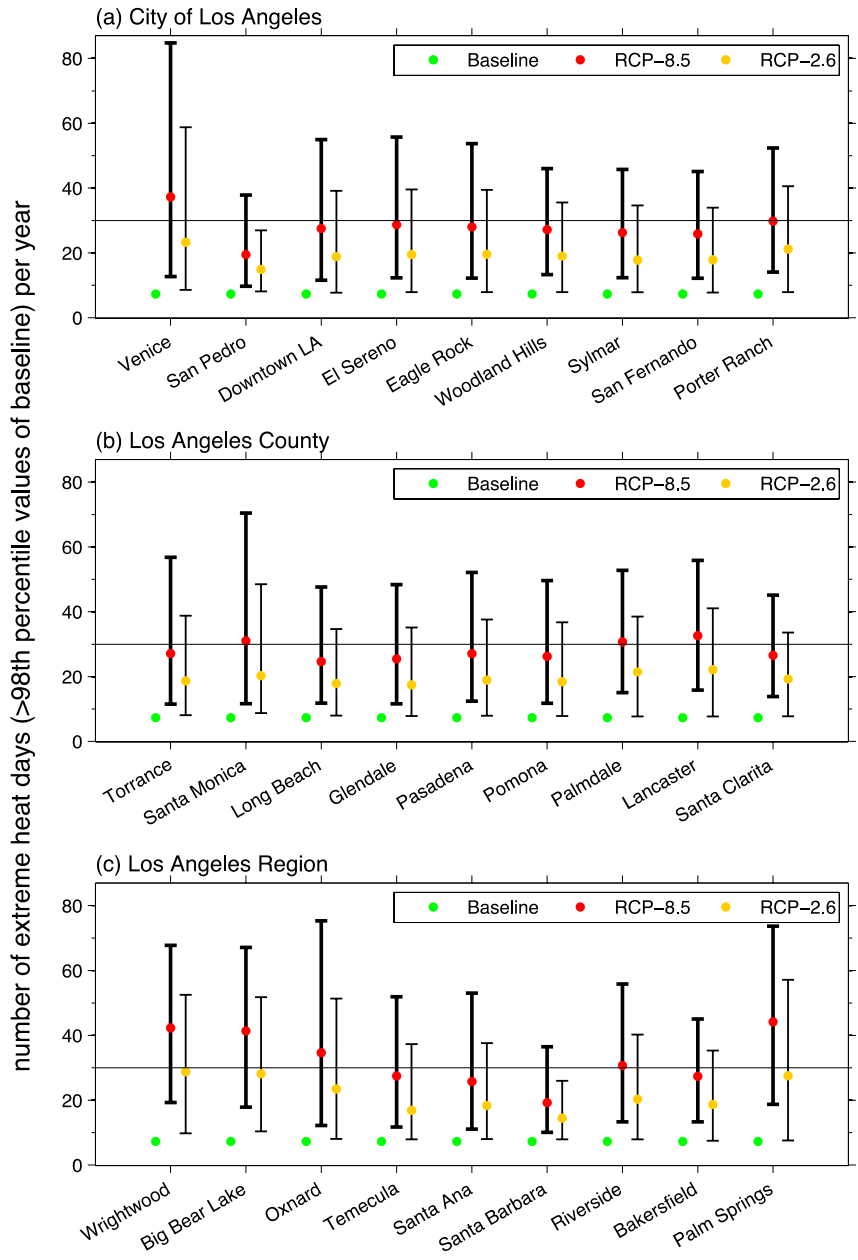
Fig. 19: Same as Fig. 18, but with a different threshold to define an extremely hot day. In this case, an extremely hot day is defined as a day in which the daily maximum temperature is greater than the 98th percentile of the daily maximum temperature PDF at that location. To aid the reader, a horizontal line corresponding to 30 days per year has been drawn on each panel.

Tables:

Table 1: Name and characteristics (country, institution, and resolution) of the 19 IPCC-AR5 GCMs used for climate downscaling. All GCMS are statistically downscaled, while only CCSM4 is dynamically downscaled. The availability of the RCP2.6 and RCP8.5 emissions scenarios is also indicated. Note: 1° is approximate 100 km.

| MODEL	COUNTRY	INSTITUTE	RESOLUTION	RCP2.6	RCP8.5
CCSM4	USA	National Center for Atmospheric Research	1.25° x .9°	✓	✓
Can-ESM2	Canada	Canadian Centre for Climate Modelling and Analysis	2.8° x 2.8°	✓	✓
CNRM-CM5	France	Centre National de Recherches Meteorologiques	1.4° x 1.4°		✓
CSIRO-Mk3.6	Australia	Commonwealth Scientific and Industrial Research Organization	1.9° x 1.9°	✓	✓
GFDL-CM3	USA	NOAA Geophysical Fluid Dynamics Laboratory	2.5° x 2.0°	✓	✓
GFDL-ESM2M	USA	NOAA Geophysical Fluid Dynamics Laboratory	2.5° x 2.0°	✓	✓
GFDL ESM2G	USA	NOAA Geophysical Fluid Dynamics Laboratory	2.5° x 2.0°	✓	✓
GISS-E2-R	USA	NASA Goddard Institute for Space Studies	2.5° x 2.0°	✓	✓
HadGEM2-CC	UK	Met Office Hadley Centre	1.9° x 1.25°		✓
HadGEM2-ES	UK	Met Office Hadley Centre	1.9° x 1.25°	✓	✓
INMCM4	Russia	Institute for Numerical Mathematics	2.0° x 1.5°		✓
IPSL-CM5A-LR	France	Institut Pierre Simon Laplace	3.75° x 1.9°	✓	✓
IPSL-CM5A-MR	France	Institut Pierre Simon Laplace	2.5° x 1.25°		✓
MIROC-5	Japan	AORI (U. Tokyo), NIES, JAMESTEC	1.4° x 1.4°	✓	✓
MIROC-ESM-CHEM	Japan	AORI (U. Tokyo), NIES, JAMESTEC	2.8° x 2.8°	✓	✓
MIROC-ESM	Japan	AORI (U. Tokyo), NIES, JAMESTEC	2.8° x 2.8°	✓	✓
MPI-ESM-LR	Germany	Max Planck Institute for Meteorology	1.9° x 1.9°	✓	✓
MRI-CGCM3	Japan	Meteorological Research Institute	1.1° x 1.1°	✓	✓
NorESM1-M	Norway	Norwegian Climate Center	2.5° x 1.9°	✓	✓

Table 2: The ensemble-mean, upper bound and lower bound of annual-mean surface air temperature change (future minus baseline, unit: °F) for districts within the city of Los Angeles, cities within Los Angeles County other than Los Angeles, and cities within our domain but outside Los Angeles County (the Los Angeles Region) for the RCP8.5 and RCP2.6 emissions scenarios.

	RCP8.5 ensemble mean	RCP8.5 upper bound	RCP8.5 lower bound	RCP2.6 ensemble mean	RCP2.6 upper bound	RCP2.6 lower bound
City of Los Angeles						
Downtown LA	3.9	6.5	1.3	2.8	5.0	0.6
San Pedro	3.8	6.3	1.2	2.7	4.9	0.5
Venice	3.7	6.2	1.2	2.7	4.8	0.5
Sylmar	4.2	6.9	1.5	3.0	5.4	0.6
San Fernando	4.2	6.9	1.5	3.0	5.4	0.6
Woodland Hills	4.3	7.0	1.5	3.0	5.4	0.6
El Sereno	4.0	6.6	1.3	2.8	5.1	0.6
Eagle Rock	4.0	6.6	1.4	2.8	5.1	0.6
Porter Ranch	4.2	7.0	1.3	2.8	5.0	0.6
Los Angeles County						
Pasadena	4.1	6.7	1.5	3.0	5.4	0.6
Pomona	4.1	6.7	1.4	2.9	5.2	0.6
Lancaster	4.9	7.9	1.4	2.9	5.2	0.6
Palmdale	4.9	8.0	1.8	3.4	6.1	0.6
Long Beach	3.8	6.4	1.8	3.4	6.1	0.6
Santa Monica	3.7	6.3	1.3	2.7	4.9	0.5
Santa Clarita	4.4	7.3	1.2	2.7	4.9	0.5
Glendale	4.0	6.6	1.6	3.1	5.6	0.6
Torrance	3.8	6.4	1.4	2.8	5.1	0.6
Los Angeles Region						
Santa Ana	3.9	6.4	1.3	2.8	5.0	0.5
Palm Springs	5.2	8.4	1.9	3.5	6.4	0.7
Riverside	4.2	7.0	1.5	3.0	5.4	0.6
Temecula	4.1	6.8	1.5	2.9	5.3	0.6
Big Bear Lake	5.2	8.3	2.1	3.7	6.6	0.8
Oxnard	3.7	6.2	1.2	2.7	4.8	0.5
Santa Barbara	3.7	6.3	1.2	2.7	4.9	0.5
Wrightwood	5.4	8.6	2.2	3.8	6.7	0.8
Bakersfield	4.5	7.3	1.6	3.1	5.6	0.6

Table 3: Average number of extremely hot days per year for districts within the city of Los Angeles, cities within Los Angeles County other than Los Angeles, and cities within our domain but outside Los Angeles County. An extremely hot day is defined as a day in which the daily maximum temperature is greater than 95°F. Results are shown for the baseline simulation, ensemble-mean, upper bound and lower bound of the RCP8.5 and RCP2.6 emission scenarios.

	Baseline	RCP8.5 ensemble mean	RCP8.5 upper bound	RCP8.5 lower bound	RCP2.6 ensemble mean	RCP2.6 upper bound	RCP2.6 lower bound
City of Los Angeles							
Downtown LA	5.6	22.9	48.1	9.9	15.8	34.1	6.3
San Pedro	1.7	5.2	10.3	2.4	3.4	7	1.9
Venice	0.1	0.6	1.4	0.1	0.3	0.8	0.1
Sylmar	53.5	96.4	122.5	67.3	81	108	55.7
San Fernando	54.4	97	124	67.5	82.1	109.2	56.1
Woodland Hills	35.6	70.9	100.5	46.9	58.3	83.4	37.1
El Sereno	12.5	40.5	74	19.2	29.4	55.4	13.3
Eagle Rock	13	41.5	73.1	20.2	29.9	55.4	13.7
Porter Ranch	55.3	99.6	124.6	70.1	85.7	110.9	58.1
Los Angeles County							
Pasadena	23.7	63.4	96.8	34.8	47.9	78.2	25.2
Pomona	28.8	69	102.6	41	54	84.6	30.6
Lancaster	54.7	95.9	118	70.2	82.5	105.1	57.4
Palmdale	36.1	77.7	104.7	51.2	62.3	89.5	38
Long Beach	4.4	16.5	32.6	6.7	11.4	22.6	4.8
Santa Monica	0.4	1.2	2.7	0.6	0.8	1.5	0.5
Santa Clarita	56.6	96.2	117.3	71.2	82.8	105.8	59.6
Glendale	19	51.7	84.2	28.1	39.2	65.6	20.2
Torrance	0.2	1.3	4	0.4	0.7	2.4	0.3
Los Angeles Region							
Santa Ana	4.5	18.3	39	7.5	12.1	26.3	5
Palm Springs	134.8	160.3	177.9	143	151.5	167.1	137.6
Riverside	57.8	103.2	127	73.1	88.7	114.4	59.7
Temecula	3.2	11.3	26.3	4.9	7.3	15.8	3.5
Big Bear Lake	0	0.6	2.9	0.1	0.1	1.2	0
Oxnard	0.1	0.6	1.9	0.2	0.3	1	0.1
Santa Barbara	4.9	12.2	23.6	6.8	9.4	17.4	5.6
Wrightwood	0	2.4	13.3	0.2	0.6	5.5	0
Bakersfield	111.3	134.6	148.9	120.2	127.7	139.6	113.6

Table 4: Similar to Table 3, but with a local temperature threshold (unit: °F) to define an extremely hot day. An extremely hot day is defined one where the daily maximum temperature is greater than the 98th percentile of the daily maximum temperature PDF at that location. By this definition the number of extremely hot days is the same at all locations (7.3 days per year). The first column gives the temperature corresponding to the 98th percentile at each location.

	Local temp. threshold	RCP8.5 ensemble mean	RCP8.5 upper bound	RCP8.5 lower bound	RCP2.6 ensemble mean	RCP2.6 upper bound	RCP2.6 lower bound
City of Los Angeles							
Downtown LA	94.5	27.6	55	11.6	18.9	39.2	7.8
San Pedro	89.9	19.5	37.9	9.7	14.9	27	8.2
Venice	84.6	37.3	84.8	12.7	23.3	58.8	8.6
Sylmar	102.9	26.3	45.8	12.4	17.8	34.7	7.9
San Fernando	103	25.9	45.1	12.2	17.9	34	7.8
Woodland Hills	100.7	27.2	46	13.3	19.1	35.6	7.9
El Sereno	96.4	28.7	55.8	12.3	19.5	39.6	7.9
Eagle Rock	96.5	28	53.7	12.2	19.6	39.5	7.9
Porter Ranch	102.5	29.8	52.4	14.1	21.2	40.6	7.9
Los Angeles County							
Pasadena	98.6	27.1	52.1	12.4	19	37.6	8
Pomona	99.5	26.3	49.6	11.8	18.4	36.8	7.9
Lancaster	103.3	32.6	55.9	15.8	22.1	41.1	7.7
Palmdale	101.3	30.7	52.8	15.1	21.5	38.6	7.7
Long Beach	93.5	24.7	47.7	11.9	17.9	34.7	8
Santa Monica	85.5	31.1	70.5	11.7	20.3	48.5	8.8
Santa Clarita	104.1	26.6	45.2	13.9	19.3	33.6	7.8
Glendale	98	25.5	48.4	11.6	17.5	35.2	7.9
Torrance	86.9	27.2	56.8	11.5	18.7	38.8	8.1
Los Angeles Region							
Santa Ana	93.8	25.8	53.1	11.1	18.4	37.6	8.1
Palm Springs	113.4	44.2	73.7	18.8	27.6	57.2	7.6
Riverside	102.3	30.8	55.9	13.4	20.3	40.3	8
Temecula	92.1	27.5	51.9	11.8	16.9	37.3	8
Big Bear Lake	83.9	41.4	67.1	17.9	28.2	51.8	10.4
Oxnard	85.7	34.7	75.3	12.2	23.5	51.4	8.1
Santa Barbara	93.3	19.3	36.5	10.1	14.5	26	8
Wrightwood	86.9	42.3	67.8	19.3	28.8	52.5	9.8
Bakersfield	112.6	27.4	45.1	13.4	18.7	35.4	7.5